

Master thesis

Calculating UV Doses and Cesium-137 Deposition in Western Norway in Relation to a Hypothetical Sellafield Accident

Gitte Helene Brunstad



Thesis submitted for the degree of
Master in Oceanography and Meteorology
60 credits

Department of Geosciences
Faculty of mathematics and natural sciences

UNIVERSITY OF OSLO

Spring 2017

Master thesis

Calculating UV Doses and Cesium-137 Deposition in Western Norway in Relation to a Hypothetical Sellafield Accident

Gitte Helene Brunstad

© 2017 Gitte Helene Brunstad

Master thesis

<http://www.duo.uio.no/>

Printed: Reprosentralen, University of Oslo

Contents

1	Introduction	5
2	Background	7
2.1	Sellafield Facility and Accidents at Similar Facilities	7
2.2	Cesium-137	8
2.3	Effects of Ionizing Radiation	8
2.4	Solar Radiation	10
2.4.1	UV Radiation	10
2.4.2	Global Radiation	10
2.5	UV Effects	11
2.5.1	Trends in Malignant Melanoma Incidences	11
2.6	Interaction Between UV and Ionizing Radiation in Organisms . .	13
3	Theory	15
3.1	Ionizing Radiation Quantities	15
3.2	UV Radiation Quantities	16
3.3	Radiative Transfer Equation	18
3.4	Parameters Affecting UV Transfer	19
3.4.1	Solar Elevation	19
3.4.2	Ozone	20
3.4.3	Turbidity	20
3.4.4	Surface Albedo	20
3.4.5	Cloud Effects	20
3.5	Transport of Radionuclides: Lagrangian Continuity Equation . .	22
3.5.1	Radioactive Decay	22
4	Methods and Data	23
4.1	SNAP Model	23
4.1.1	Weather Scenario	23
4.1.2	Parameterizations	24
4.1.3	Input and Assumptions	26
4.2	The libRadtran Package	27
4.2.1	Disort Solver	27
4.2.2	Input and Assumptions	27
4.3	Clouds: The Lindfors Method	30
4.3.1	Global Radiation Data	31

5	Results	33
5.1	Cs-137 Accumulated Wet Desposition	33
5.2	Cs-137 Accumulated Dry Desposition	33
5.3	Cs-137 Deposition for Selected Stations	34
5.4	Sum of Cs-137 Deposition For Selected Stations	36
5.5	Time Development of Deposition	36
5.5.1	Fureneset	36
5.5.2	Flesland	36
5.5.3	Særheim	37
5.6	Daily UV Dose (SED) After Deposition	37
5.7	Cloud Effects on UVI Maximum	37
5.8	UV Index at Fureneset, Flesland and Særheim for Selected Days	39
5.9	Performance of Lindfors Method	41
6	Discussion and Future Perspectives	46
	References	52
	Appendices	53
A	Daily UVI Plots for Fureneset, Flesland and Særheim	54
B	Daily UVI Plots for Florida	69

Abbreviations

SNAP	S evere N uclear A ccident P rogram
ARGOS	A ccident R eporting and G uiding O perational S ystem
libRadtran	l ibrary of R adiative t ransfer
CIE	C ommision I nternationale de l' E clairage (International Commission on Illumination)
NRPA	N orwegian R adiation P rotection A uthority
UV	U ltraviolet
SZA	S olar Z enith A ngle
ABL	A tmospheric B oundary L ayer
BCC	B asal C ell C arcinoma
SCC	S quamous C ell C arcinoma
CMF	C loud M odification F actor
NWP	N umerical W eather P rediction
HIRLAM	H igh R esolution L ocal A rea M odelling
HAL	H ighly A ctive L iquor
MED	M inimum E rythema D ose

Acknowledgements

I want to thank my external supervisors, Terje Christensen and Martin Album-Ytre Eide at the NRPA, for letting me take part in the work done in relation to Umbrella 7: Doses and Effects of Ultraviolet and Ionizing Radiation at CERAD, a Centre of Excellence. Thank you for inviting me to the joint Euroskin, NOF-FOF and CERAD seminar in Bergen 3.-4. November 2016.

Thank you to my internal supervisor Terje Koren Berntsen for helping me get on the right track and for providing helpful input.

I also want to thank:

- Heiko Klein at met.no, for helping me set up the SNAP model and providing me with HIRLAM forecasts
- Bjørn Johnsen at NRPA in providing me with ozone concentrations and UV measurements
- Anders Lindfors for letting me use his UV reconstruction model

Thanks to friends and family for having faith in me, and providing invaluable support during this challenging project – you know who you are.

Chapter 1

Introduction

After the Chernobyl accident in 1986, much effort has been put down to describe the distribution and consequences of radioactive releases, adding to the natural background levels. The effort has often been related to possible accidents at nuclear installations. Similarly, UV radiation exposure has got increased attention, particularly in countries with large natural variations, such as Norway. Variations in ozone layer concentrations and the increasing number of malignant melanoma incidents among the Norwegian population has caused concern in the public and in scientific research communities. Today UV-maps have been established, showing forecasted UV exposures (J/m^2) over Norway in order to make the population more aware of which protective measures are advised to avoid harmful UV effects. Daily UV forecasts are available at yr.no.

While considerable effort to assess the distribution and the consequences of each of these two components has been laid down, little effort has been used to consider these two components simultaneously, for example related to accidental release of radioactivity. This thesis will, using a Lagrangian transport model developed for nuclear accidents, and a method for reconstructing UV irradiance, investigate how the atmosphere affects both transport of radioactive isotopes and transfer of UV radiation related to a hypothetical Sellafield accident. Sensitivity tests regarding the dimensions of nuclear plume will be performed. For the simulations of UV irradiance, global radiation measurements have been exploited to account for cloud effects on the level of UV radiation.

Synergistic and antagonistic effects regarding radiation have been investigated in detail by Tyrrell [1978]. Countless factors may affect the response to radiation and interaction between radiation exposure, but in this thesis we have based our work on the interaction between UV and ionizing radiation, in accordance to Umbrella 7: *Doses and Effects of Ultraviolet and Ionizing Radiation* at CERAD (Centre of Environmental Radioactivity). The interaction between ionizing radiation and UV radiation is complicated and may vary significantly depending on the order of the exposure, the exposure dose, the interval between the exposures the target of the radiation effect and defence and repair capacities of different organisms. The combined effects will be discussed in Section 2.6. Ongoing work at CERAD is trying to uncover the biological interaction processes.

Since UV radiation and ionizing radiation have significantly different properties, these topics will be introduced separately in Chapter 2. After a description of nuclear accidents, the radionuclide cesium-137 and effects of ionizing radiation exposure, we will change perspective over to UV radiation and UV effects. Our main concern in this thesis is how the state of the atmosphere affects both the radiative transfer of UV and the long-range transport of radionuclides. A large portion of Chapter 3 will therefore describe transfer and transport, and look at which parameters and mechanisms influence these processes.

In Chapter 4, the SNAP model and libRadtran package used for simulating transport of radionuclides and radiative transfer respectively, will be presented, as well as which assumptions were made and which input data was given. Clouds have a significant impact on the amount of UV radiation reaching the surface, and therefore must be accounted for in the libRadtran simulations. Since hourly values of global radiation data are available at several weather stations in the hypothetical deposition area, the Lindfors method was deemed the best option for doing this [Lindfors et al., 2007]. In this method, the information on how clouds affect global radiation, is converted and applied to the UV range. The Lindfors method is described in more detail in Section 4.3.

The work done in this master project, represents the first step towards providing a system to quantify the synergistic biological effects of ionizing radiation and UV doses. Given the necessary limitations of a master project, the focus of the thesis has been on atmospheric models needed to calculate the Cesium-137 deposition and UV doses. Remaining work beyond the scope of the thesis include applying models for biological uptake of Cesium-137 and calculating long term UV and ionizing radiation doses.

Chapter 2

Background

2.1 Sellafield Facility and Accidents at Similar Facilities

In this thesis, the Sellafield facility is referred to as the storage facilities for liquified high-level radioactive waste. The complete site comprises a number of different functions related to the front and the back end of the nuclear fuel cycle. Major safety concerns have been expressed related to the Highly Active Liquors (HALs) in a number of storage tanks, before the material is vitrified (processed into stable solid forms) for transport and long term storage. The HAL waste is considered highly dangerous and produces significant amounts of heat. It needs to be cooled and stirred continuously in the tanks to avoid overheating.

The safety conditions at Sellafield have caused concern among authorities and environmental organizations for many years, and the recent Panorama investigation and newly released BCC documentary from 2016 revealed that conditions are worse than first feared. A former senior manager has expressed that he's worried about a fire breaking out in the HAL waste, resulting in a plume of radioactive waste that can spread across parts of Europe [Quinn, 2016].

The risk associated with the handling of HAL at Sellafield corresponds with an earlier accident at a similar type of facility in Russia in 1957, known as the Kyshtym disaster. The Kyshtym disaster, taking place 29 September in 1957 at the Mayak fuel reprocessing plant in former Soviet Union, is considered a level 6 nuclear accident [INES, 2008], making it the third most serious nuclear accident ever recorded, behind the disasters of Fukushima and Chernobyl.

In 1957, the cooling system in one of the tanks containing 70-80 tons of HAL waste, failed and was not repaired. Rising temperatures lead to evaporation and a chemical explosion in the dried waste. The explosion, estimated to have a force of about 70-100 tons of TNT, threw the concrete lid up into the air and lead to a release of 740 PBq of radioactivity [Ytre-Eide et al., 2009]. Most of the contamination happened near the site and lead to pollution of the Techa River, but a plume containing 80 PBq of radionuclides spread out over hundreds of square kilometers. The fallout from the cloud of radionuclides resulted in a long-

term contamination of an area larger than 20,000 km², mainly by Cesium-137 and Strontium-90. This area is often referred to as the East-Ural Radioactive Trace.

2.2 Cesium-137

In this study, we limit the number of isotopes included to Cesium-137 (Cs-137). There is a large number of isotopes that are released and relevant regarding environmental and health consequences, however, cesium-137 is often considered in particular detail. Cesium-137 is considered because of its long half-life of 30.17 years [Unterweger, 2002] and high water solubility – it is easily transferred from a release through the environment and thereafter distributed in the body, especially in muscle tissue. In most biological systems, cesium-137 behaves like Potassium because of its resemblance in both size and chemical characteristics [Harbitz and Skuterud, 1999].

Cesium-137 is a cleavage product in the nuclear fission of uranium. By emitting β -particles, it gives barium-137. Barium-137 is generated in an excited state, i.e. metastable, and will first become stable after emitting γ -radiation, see Fig. 2.2. The half-life of metastable barium-137 is only 2.55 minutes. Since this decay process happens so rapidly, both β - and γ -emission is associated with cesium-137 decay from a simplified perspective.

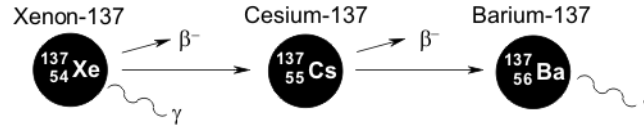


Figure 2.1: Decay of Cesium-137 [geigercounter.org, 2017].

Strontium-90 (Sr-90) has a half-life of similar extent as Cs-137: 29 years. Since the focus of the thesis is to investigate how the atmosphere affects the transport and deposition of radionuclides when varying the plume height and size of the isotopes, we limit ourselves to one isotope. In the atmosphere, Cs-137 and Sr-90 behave much the same way, and therefore considering both isotopes will only scale the resulting fallout. Looking at the differences in pathways and calculating possible doses for different radionuclides is beyond the scope of this thesis. If we were to look at the consequences of a hypothetical Sellafield accident for the Norwegian population in detail, as NRPA has done previously [Ytre-Eide et al., 2009] for Cs-137, the choice of radionuclides would be important due to different behaviours in biological systems and differences in biological half-lives.

2.3 Effects of Ionizing Radiation

Exposure to ionizing radiation can potentially result in short-term and long-term effects in every organ system in the body. Updated reviews of the research on the effects of radiation exposure are regularly presented by UN, represented

by UNSCEAR, based on the efforts of the International Commission on Radiological Protection (ICRP) and the International Atomic Energy Agency (IAEA).

At a molecular level, the primary consequence of radiation exposure is cell damage, either fully repaired, or on the other hand, dysfunction, carcinogenesis or cell death. The scope of the damage depends on numerous variables, such as type of exposure (total or partial exposure, internal or external contamination), the type of tissue (sensitive to radiation or not), the type of radiation (e.g. γ , β , α) and its energy [UNSCEAR, 1996]. The total absorbed dose, in addition to the dose rate, is the measure associated with describing the overall risk. Quantities for measuring ionizing radiation doses are described in Section 3.1.

Accute sickness can occur when most of the human body is exposed to a single dose of more than 1 Gy. This has never been relevant with respect to the general population in association with nuclear accidents. However, in relation to the Chernobyl accident, the highest absorbed dose in a worker was above 10 Gy, resulting in symptoms of acute radiation syndrome [Mettler Jr et al., 2007]. Comparably, the exposure of the local inhabitants before the accident constituted around 1 mSv pr. year, and this increased significantly as a result of the accident, with more than 50%. For a large number of the local population, this resulted in evacuation and subsequent re-location. The deposition levels causing such exposure levels is $\sim 10^5$ Bq/m² and above, heavily dependent on which isotopes considered and possible exposure pathways. For population in Norway, the possible exposure was heavily dependent on dietary routines, often closely connected with certain cultural traditions (e.g. consumption of reindeer in the Lapp population [Harbitz and Skuterud, 1999]). The consumption of one kg meat, with 600 Bq/kg, would correspond to a dose of 0.0078 mSv. Thus, any consideration of potential health effects after such exposure depends on how one statistically considers the consequences of tiny individual doses by a large number of exposed people.

2.4 Solar Radiation

The sun emits radiation that can be approximated by a black body with a temperature of approximately 5525 K (5250 °C). The spectral distribution of the emission can be described by Plank's law. Therefore 99% of the solar radiation lies in the wavelength interval 200-4000 nm, as illustrated in Figure 2.2.

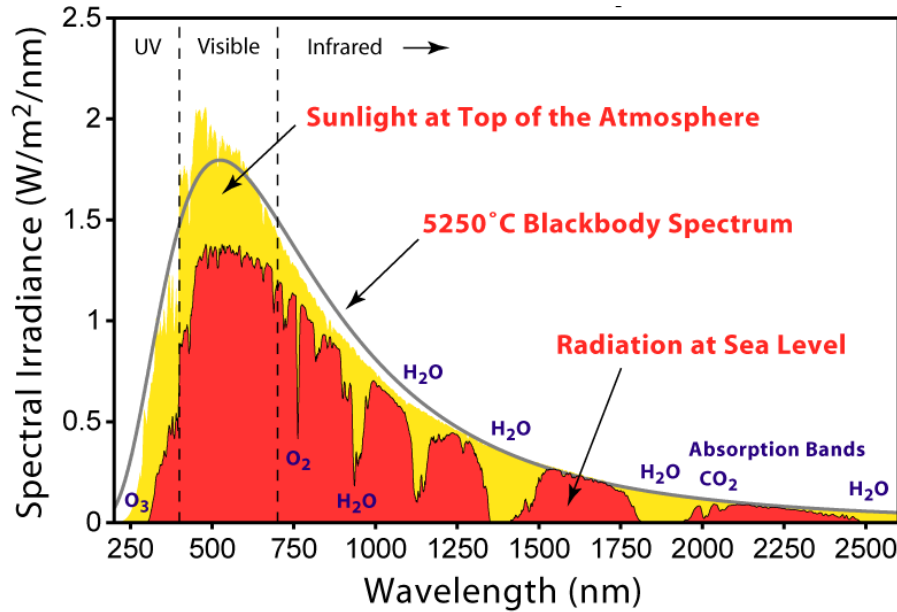


Figure 2.2: The Solar Radiation Spectrum created by Rohde [2007] for Global Warming Art project. The absorption bands for important atmospheric gases are indicated.

2.4.1 UV Radiation

Ultraviolet (UV) radiation is the radiation in the wavelength interval 100-400 nm. Although UV radiation only amounts to a small percentage of the emitted solar radiation [Johnsen et al., 2013], UV photons possess enough energy to cause photochemical changes in molecules and cell structures. It is therefore an important component of the solar radiation spectrum. The Ozone layer and water vapour absorb all the solar UVC radiation (100-280 nm), so none of it reaches the Earth's surface. The solar UV radiation mainly consists of UVA (320-400 nm). However, UVB radiation is important since these wavelengths are most efficient in producing several biological effects such as erythema (sunburn), see Section 3.2.

2.4.2 Global Radiation

The term global radiation describes the total amount of solar radiation (direct and diffuse) received by the surface. The wavelength interval for global

radiation typically spans from approximately 300 nm to 3000 nm, and therefore includes UV radiation, visible light and infrared radiation. At Norwegian weather stations, the global radiation range is 285-2800 nm.

2.5 UV Effects

UV radiation has various acute and chronic effects on the human skin, eye and immune system [SCCP, 2006]. One of the most common effects is erythema, often referred to as sunburn, which leads to reddening of the skin. Erythema is caused by increased blood flow to the affected skin, and peaks between 8 and 24 hours after exposure. The underlying cause is direct and indirect cell damage through the generation of reactive oxygen species. DNA-damage and activation of inflammatory mechanisms are thought to trigger this reaction, and will eventually lead to a widening and swelling of the blood vessels [Naylor, 1997].

Erythema is associated with skin cancer, especially if the erythematous exposure happens early in childhood [SCCP, 2006]. Skin cancer is the most severe UV effect, and can be divided into two categories: non-melanoma skin cancer and malignant melanoma. The two types of non-melanoma skin cancer are basal cell carcinoma and squamous cell carcinoma. Both occur in the outer layer of the skin, usually in sun-exposed areas like the head and neck. Basal cell carcinoma accounts for 80% of the cases of skin cancer, but grows slowly and is unlikely to spread to other parts of the body. Squamous cell carcinoma is more likely to spread, but this is uncommon. Even though malignant melanoma accounts for only 4% of the cases, it is the main cause of death from skin cancer [SCCP, 2006]. Melanoma caused a total of 327 deaths in Norway in 2013 [Cancer Registry of Norway, 2015]. This form of cancer develops from melanocytes, the cells that produce pigmentation, and the disease is characterized by changes in mole size, colour and/or shape.

UV radiation is an important source of vitamin D in sunny countries and in the summer at northern latitudes. Alternative vitamin D sources are dietary: marine oil from fat fishes, eggs and vitamin D fortified food products. Vitamin D is important for skeletal health through calcium regulation, but may also play a crucial role in preventing colon, breast and prostate cancer and certain autoimmune diseases such as multiple sclerosis and Type 1 diabetes [Webb and Engelsen, 2006].

2.5.1 Trends in Malignant Melanoma Incidences

Since the 1970s, there has been a strong increase in incidence of both malignant melanoma and non-melanoma skin cancers among Norwegians. In 1954-1958 the number of melanoma incidents were 2.3 and 2.0 cases pr. 100,000 for men and women respectively, in 2013 malignant melanoma incidence exceeded 20 cases pr. 100,000 for both genders, see Fig. 2.3. This trend is strongly related to a change in sunbathing habits and more widespread use of solariums [WHO, 2002]. To make the public more aware of the UV radiation doses they are receiving, and to encourage to take necessary protective measures to avoid negative UV

effects, the UV index has been developed. Quantities for measuring UV and UV index will be explained in Section 3.2.

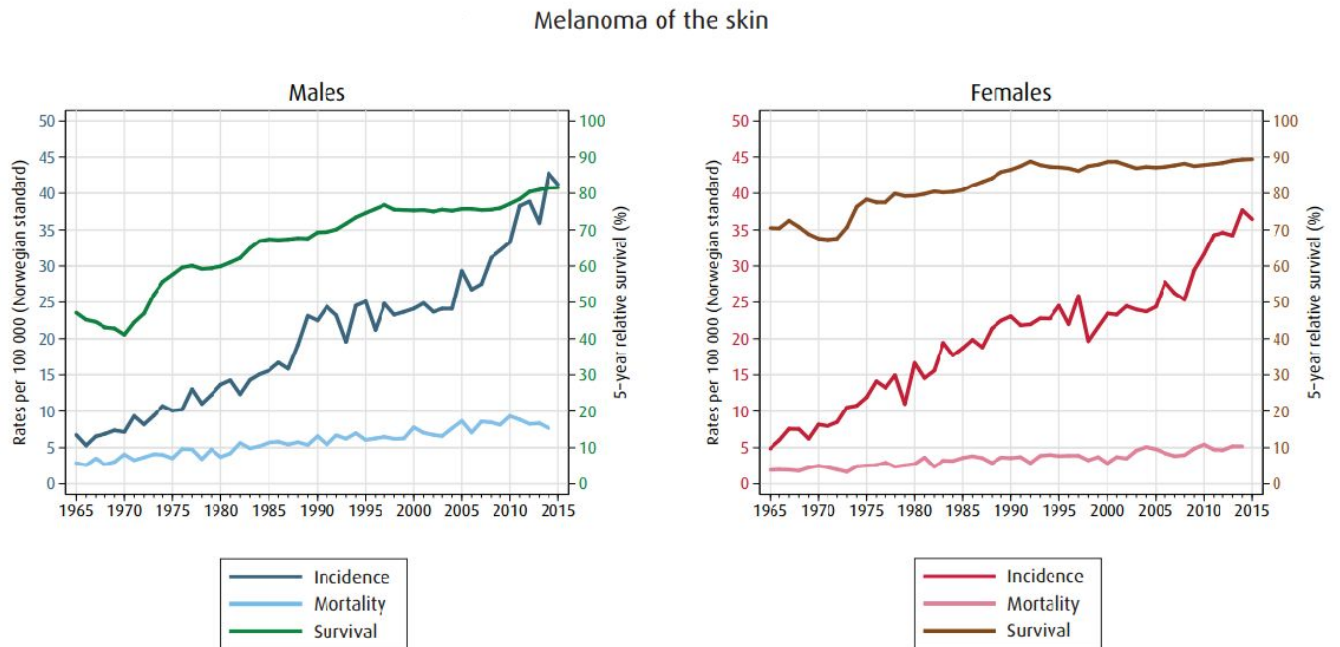


Figure 2.3: Incidence, mortality and survival for malignant melanoma [Cancer Registry of Norway, 2015].

2.6 Interaction Between UV and Ionizing Radiation in Organisms

The effect of exposure to both ionizing radiation and UV radiation is complicated and depends on numerous factors including magnitude of dose, the order of irradiation, the time interval between the exposures and the organisms' repair system of radiation induced injuries. In this section we will present some of the results found in biological research to support our motivation for looking at a nuclear accident from a UV perspective.

In cell survival theory, the amount of surviving cells depend on the number of radiation induced double-strand breaks in the DNA molecule. Single-strand breaks can be repaired and are therefore not lethal. However, two independently induced single-strand breaks combined may give a double-strand break.

The mean number of double-strand breaks in DNA induced by ionizing radiation is given by: $N = \alpha_0 D + \beta_0 D^2$ where α_0 represents the chance for a double-strand break per unit dose for one radiation event, and $\beta_0 D^2$ expresses the chance of single-strand breaks being combined to form a double-strand break. D signifies the ionizing radiation dose.

As mentioned in the section on UV effects, UV radiation is a DNA-damaging agent, and it therefore has the ability to cause single-strand breaks. The mean number of double-strand breaks, i.e combined pairs, can be expressed as kX^2 where X represents the UV exposure.

In their analysis, Leenhouts and Chadwick [1978] proposed that the total effect of UV and ionizing radiation on cell survival could be expressed as:

$$S = \exp [-p (\alpha_0 D + \beta_0 D^2 + \alpha' k' X D + k X^2)] \quad (2.1)$$

This expression for cell survival accounts for the synergistic effect arising since single-strand breaks induced by either ionizing radiation or UV radiation can be combined to give additional double-strand breaks, represented by the term $\alpha' k' X D$, illustrated in Figure 2.4. The coefficients α' and k' are associated with the number of single-strand breaks induced by ionizing radiation (α'') and UV radiation (k'') respectively.

In response to UVA and UVB radiation, keratinocytes produce nitric oxide (NO) [Roméro-Graillet et al., 1997]. Cook et al. [2004] reported that NO and ionizing radiation can synergistically activate the tumor suppressor p53 in colorectal cancers in mice. Thus, in some cases, UV irradiated cells can be more resistant towards other radiative exposure. However, other studies report an opposite effect on tumors. Lerche et al. [2013] found significantly faster tumor development in hairless mice that were irradiated by both UV and ionizing radiation. The mice were exposed to simulated solar radiation both prior to and after x-ray irradiation.

In epidemiological studies on skin cancer on the scalp and face of children following radiotherapy treatment for tinea capitis (scalp ringworm), Kleiner-

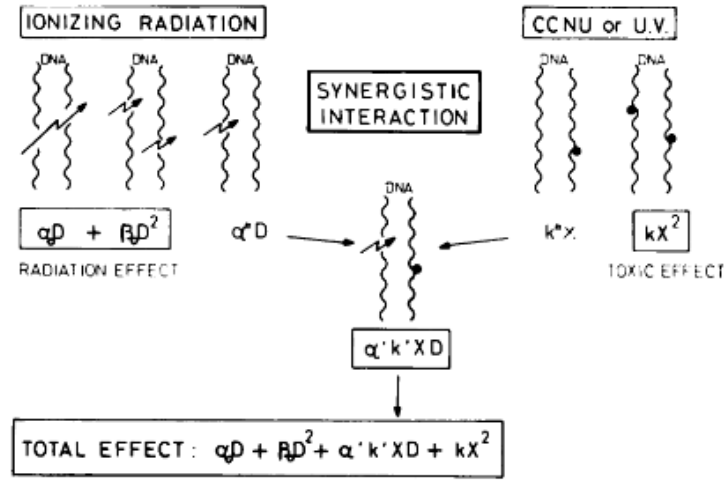


Figure 2.4: Total Effect of Ionizing Radiation and UV Exposure [Leenhouts and Chadwick, 1978].

man [2006] found significantly increased risks after ionizing radiation exposure, for basal cell cancers (BCCs) only. The minimum latency period was 20 years. Since there was a predominance of skin cancers in sun-exposed areas and hardly any cases where diagnosed in dark-skinned children who received the same exposure, an interaction between ionizing radiation and UV radiation was suggested.

UV-exposure is a well-established cause for skin cancer, but ionizing radiation is also associated with non-melanoma skin cancers. In addition to increased risk for non-melanoma skin cancer being detected in radiologists, uranium-miners and patients treated for tinea capitis in childhood, non-melanoma skin cancer is also one of the cancer types most strongly associated with the atomic bombing of Hiroshima and Nagasaki [Thompson et al., 1994]. Since skin cancer is an affliction shared by UV and ionizing radiation, it is natural to wonder to what extent the carcinogenic pathways of each agent affect each other.

Chapter 3

Theory

3.1 Ionizing Radiation Quantities

Radioactivity is given in the unit becquerel (Bq). One becquerel accounts to an activity of one nucleus decay per second in a radioactive material. The SNAP model used for modelling transport after hypothetical nuclear accidents, returns deposition concentrations of radioactivity given in Bq/m², and surface air concentrations in Bq/m³. In this thesis we will focus on the Cs-137 deposited on the ground in units of Bq/m².

Using the deposition values to perform dose calculations is beyond the scope of the thesis. However, the motivation behind the thesis is comparing UV and ionizing radiation doses. Therefore a basic description of ionizing radiation doses is provided below to maintain consistency.

Gray is a derived unit for the absorbed ionizing radiation dose, D, and is defined as the absorption of one joule of radiation energy per kilogram of matter:

$$1 \text{ Gy} = 1 \text{ J/kg}$$

Sievert is a dose unit used to describe the health effects of low-level ionizing radiation on the human body. The equivalent dose, H, is measured in Sievert (Sv):

$$H = D \cdot w_R \text{ [Sv]}$$

w_R is the weighting factor which takes into account that different types of ionizing radiation give different biological effects. α -particles are assumed to have biological effect that is twenty times greater than that of β -particles and γ -radiation.

The effective dose, E, is also measured in Sievert. This is the sum of the doses to all the organs in the body, the “whole body dose”, and takes into account that different organs and tissues have varying sensitivity to ionizing radiation. Effective dose is given by:

$$E = \sum^{\text{organ}} H \cdot w_T \text{ [Sv]}$$

where w_T is the weighting factor which accounts for the different organs' sensitivity to ionizing radiation.

3.2 UV Radiation Quantities

UV radiation can be measured as irradiance or radiance [Thomas and Stamnes, 2002].

Spectral irradiance (radiative flux), F_λ , is the radiant energy flux received by a surface per unit area dA per unit wavelength $d\lambda$. Q denotes the radiant energy.

$$F_\lambda = \frac{Q}{dA d\lambda} \text{ [Wm}^{-2} \text{ nm}^{-1}\text{]}$$

Spectral radiance (intensity), I_λ , is the radiant energy flux received by a surface, per unit solid angle per unit area dA per unit wavelength $d\lambda$:

$$I_\lambda = \frac{dQ}{\cos \theta dA d\omega d\lambda} \text{ [Wm}^{-2} \text{ sr}^{-1} \text{ nm}^{-1}\text{]}$$

Radiance and irradiance is related in the following way:

$$F_\lambda = \int_{4\pi} d\omega \cos \theta I_\lambda \text{ [Wm}^{-2} \text{ nm}^{-1}\text{]}$$

UV Index and Erythral Action Spectrum

The UV index has been adopted and standardized by the World Health Organization (WHO), World Meteorological Organization (WMO) and other contributors to spread awareness of the risks of UV radiation and help people take necessary protective measures. The UV index is a dimensionless measure, expressed as an integer, of the erythral strength of UV radiation on a horizontal surface, and ranges between 0 during winter darkness to approximately 14 in the middle of the day at the equator. All values exceeding 11 are considered extreme. To obtain the UV index, the solar spectrum, $F(\lambda, t)$, is multiplied with the CIE standard erythral action spectrum, $A(\lambda)$, and integrated over wavelength. The action spectrum indicates which wavelengths are effective in producing erythema. Further, we multiply by $40 \text{ (W/m}^2\text{)}^{-1}$ to obtain suitable number to present to the public. The weighting of the solar spectrum is shown in Equation 3.1 and Fig. 3.1. Safety measures have been recommended for different values of the UV index, and involve using clothing, sun screen, sunglasses and shade as protection when UVI exceeds 2.

$$\text{UVI} = 40 \text{ (W/m}^2\text{)}^{-1} \int_{\lambda=285 \text{ nm}}^{\lambda=400 \text{ nm}} A(\lambda) F(\lambda, t) d\lambda \quad (3.1)$$

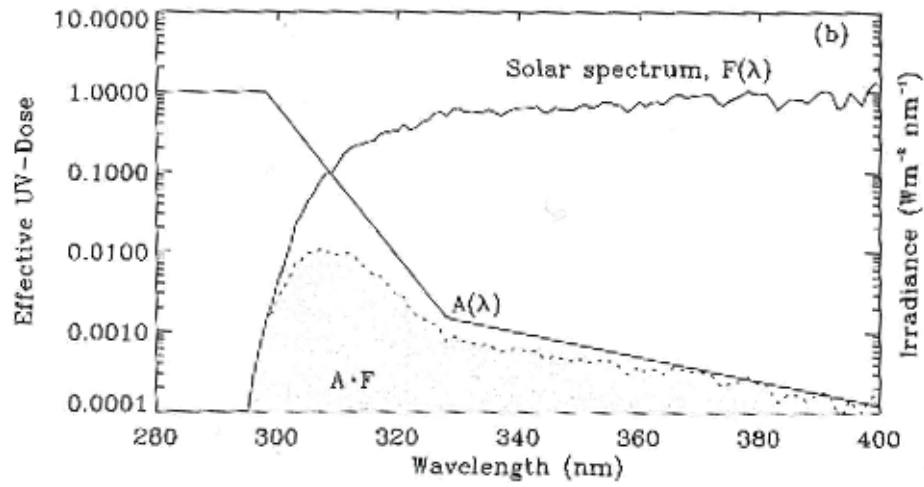


Figure 3.1: Weighting the Solar Spectrum with the Action Spectrum for Erythema [Thomas and Stamnes, 2002].

Erythelial Doses: SED and MED

Erythema is dependent on skin type: Fair-skinned people have greater susceptibility for erythema than those with darker skin. To account for differences between skin types, a standard erythelial dose unit (SED) and minimal erythelial dose unit (MED) was defined by the CIE. SED is a measure of the erythema effective UV exposure, and 1 SED is equivalent to 100 Jm^{-2} erythema effective radiation [Webb et al., 2011]. MED measures individual sensitivity to erythema, and is estimated to be 1-3 SED for white skinned individuals with skin types I and II, see Table 3.1. However, there are individual differences within each skin type, so the MEDs presented are only indicative.

Table 3.1: Classification of skin phototypes based on susceptibility to erythema and indicative MEDs for unacclimatized skin [SCCP, 2006].

Skin Phototype	Sunburn susceptibility	Tanning ability	Classes of Individuals	1 MED (measured in SED)
I	High	None	Melano-comprised	1-3
II	High	Poor		
III	Moderate	Medium	Melano-competent	3-7
IV	Low	Dark		
V	Very low	Natural brown skin	Melano-protected	7-> 12
VI	Extremely low	Natural black skin		

3.3 Radiative Transfer Equation

The amount UV radiation that reaches the surface is determined by solving the radiative transfer equation (RTE), Eq. 3.2. The RTE expresses that when a beam of solar radiation travels through the atmosphere, it loses radiative energy to absorption, gains energy by emission and redistributes energy by scattering.

$$\frac{dI_\lambda}{d\tau_s} = \underbrace{-I_\lambda}_{\text{sink}} + \underbrace{[1 - a(\lambda)]B_\lambda(T) + \frac{a(\lambda)}{4\pi} \int_{4\pi} d\omega' p(\hat{\Omega}', \hat{\Omega}) I_\lambda(\hat{\Omega}')}_{\text{source}} \quad (3.2)$$

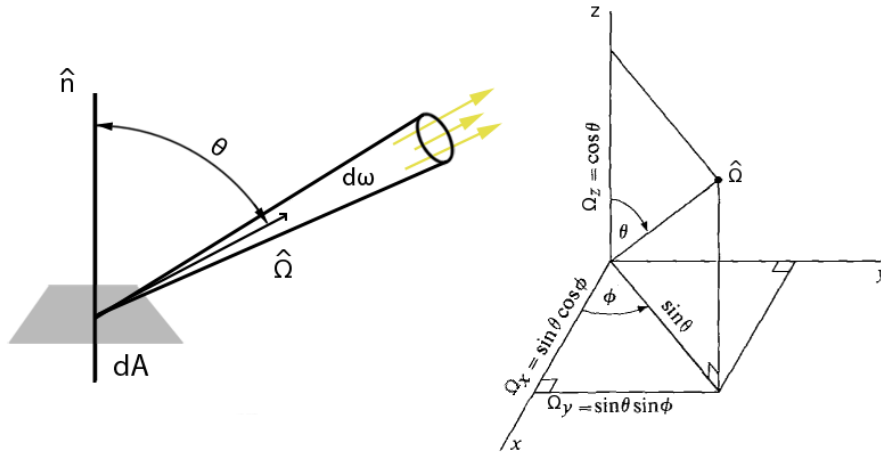


Figure 3.2: Illustration of solid angle

I_ν : Spectral intensity/radiance

$p(\hat{\Omega}', \hat{\Omega})$: Scattering phase function

$B_\nu(T)$: Black body spectral intensity/radiance at temperature T

τ_s : slant optical path

$a(\nu)$: Single-scattering albedo

$d\omega = d\phi d\theta \sin \theta$: Solid angle centered around direction $\hat{\Omega}$. Fig. 3.2.

θ : angle between the unit normal \hat{n} and $\hat{\Omega}$. See Fig. 3.2.

(' is used to indicate the solid angle of incidence and incidence direction)

The source term expresses the amount of radiative energy which is directed into the solid angle $d\omega$. The two sources are thermal emission from an absorbing medium, and radiative energy being scattered into $d\omega$ from all incidence angles: The scattered radiation in $d\omega$ could either be scattered once (single scattering) or multiple times. $a(\nu)$ is called the single-scattering albedo, and is interpreted as the probability of scattering per extinction event, whereas the co-albedo $(1 - a(\nu))$ can be interpreted as the probability of absorption per extinction event. The surface temperature and the temperatures in the atmosphere are not high enough to give emission of UV radiation, so B will be zero

when modelling UV irradiances. Therefore the only source of UV is from scattering. The sink term is loss of radiative energy from dw due to scattering and absorption.

Since it is convenient to use plane-parallel geometry to describe radiative transfer in the atmosphere, we want to apply the vertical optical path τ (optical depth), instead of the slant path τ_s . If we also take into account that the solid angle $d\omega$ can be written as $d\phi d\theta \sin \theta$ and separate the scattering term in two: single scattering and multiple scattering, the radiative transfer equation can be rewritten in the following way:

$$\begin{aligned} u \frac{dI_\nu(\tau, u, \phi)}{d\tau} = & \overbrace{I_\nu(\tau, u, \phi)}^{\text{extinction}} - \overbrace{\frac{a(\nu)}{4\pi} \int_0^{2\pi} d\phi' \int_{-1}^1 du' p(u', \phi'; u, \phi) I_\nu(\tau, u', \phi')}^{\text{multiple-scattering}} \\ & - \overbrace{[1 - a(\nu)] B_\nu(T)}^{\text{emission}} - \overbrace{\frac{a}{4\pi} p(-u_0, \phi_0; u, \phi) F^s e^{-\tau/\mu_0}}^{\text{single-scattering}} \end{aligned}$$

u : $\cos \theta$

ϕ : azimuth angle

u_0, ϕ_0 : cosine of incident solar zenith angle, solar azimuth angle

F^s : solar flux

$\mu_0 = |u_0|$

The RTE is an integro-differential equation which relates the spatial derivative of the radiance to an angular integral over the local radiance. To obtain the radiance, we therefore need to solve for a function which depends on three variables: The optical depth τ , u and the azimuth angle ϕ . However, in slab geometry, irradiance only depends on the azimuthally averaged radiance.

To shorten the computation time when solving the RTE numerically, the integral on the right hand side of the RTE is replaced by a sum over discrete ordinates. The Discrete Ordinates Method will be explained in Section 4.2.

3.4 Parameters Affecting UV Transfer

3.4.1 Solar Elevation

The most important factor affecting the amount of UV radiation, is the elevation of the sun above the horizon which varies with latitude, season and time of day [Johnsen et al., 2013]. When the sun is high in the sky, the pathway for the solar beams is shorter and they are less likely to be scattered or absorbed by gases and particles in the atmosphere. Low solar elevation results in a longer pathway through the ozone layer and more UVB will be absorbed, resulting in a solar spectrum which is less erythemogenic. Other factors that must be taken into account are cloud cover, surface albedo, temporal variations in the ozone layer and turbidity.

3.4.2 Ozone

Ozone has several absorption bands in both the UV, visible and in the infrared regions. The absorption strength in the bands depends on the total amount of ozone. In the UV region, the shortest wavelengths are absorbed in repeated absorption processes. The ozone layer is almost opaque for wavelengths up to approximately 290 nm. For wavelengths above 290 nm, the attenuation decreased rapidly, and for wavelengths above 350 nm, the ozone layer becomes transparent [Iqbal, 2012]. If ozone content decreases, less collisions between ozone and UV photons will occur, and a smaller portion of UV radiation is absorbed.

3.4.3 Turbidity

The turbidity of the air due to aerosols affects the absorption and scattering of UV radiation. UV attenuation is greatest when there is a large number of small particles present [Iqbal, 2012]. Aerosol turbidity is highly variable in time and space, ranging from clean air to heavily polluted. Anthropogenic pollution, desert dust, biomass burning and volcanic eruptions contribute to this. Most of the aerosols are located in the troposphere.

3.4.4 Surface Albedo

Albedo is the reflectivity coefficient of a surface, and is defined as the ratio of the reflected radiation to the incident radiation. The albedo is therefore dimensionless and has values between 0 (black surface, none of the radiation is reflected) and 1 (white surface, all the radiation is reflected).

Albedo is dependent of wavelength, and in general albedo is smaller for shorter wavelengths. For bare soil, the albedo is approximately 5% within the UV range. In general the albedo for UV radiation is low, with slight variations depending on whether the surface is dry or wet, and whether the surface is covered by vegetation or concrete [Feister and Grewe, 1995, McKenzie et al., 1998, Lenoble et al., 2004].

However, if the ground is covered by snow, the albedo can approach 90%, depending on the snow's composition and age, and enhance the UV irradiance significantly [McKenzie et al., 1998]. This enhancement is due to that some of the reflected radiation will be scattered back towards the surface by Rayleigh scattering. In this thesis, we measure UV irradiances at a time of year with snow-free conditions and will therefore assume that the albedo is 0.05.

3.4.5 Cloud Effects

In general, clouds attenuate UV irradiance. For overcast conditions, UV radiation will be reflected between the ground and cloud base, the cloud top and the atmosphere and between different cloud layers, and is therefore less likely to reach the ground. For scattered clouds, the edges of the clouds can reflect

UV radiation as well. In the cases where the solar disk is visible, reflection from the edges of the cloud can enhance the diffuse component in such a way that the UV irradiance exceeds the clear sky-value, sometimes referred to as UV enhancement [Josefsson and Landelius, 2000]. The visibility of the solar disc during partly cloudy conditions has great impact on the cloud effect for certain cloud types. Estupiñán et al. [1996] reported that cumulus-type clouds can attenuate up to 99% of the total UVB radiation during overcast conditions. However, for partly overcast conditions with cloud linings reflecting radiation, these same type of clouds were also found to increase localized UVB radiation with up to 27% over time scales less than an hour.

High level clouds are more transparent than medium and low level clouds. In addition, precipitating clouds are more opaque than non-precipitating clouds – as expected [Josefsson and Landelius, 2000]. Low cumulonimbus clouds can have an optical thickness which is 1000 times greater than that of cirrus cloud [Koepke et al., 2002]. To measure the influence of clouds on UV radiation, the cloud modification factor (CMF_{UV}) has been introduced [Calbo et al., 2005]. CMF_{UV} is the ratio between the UV irradiance for clear sky conditions and the UV irradiance for cloudy conditions:

$$\text{CMF}_{\text{UV}} = \frac{I_{\text{UV-cloudy}}}{I_{\text{UV-clear}}}$$

For cirrus clouds the cloud effect is marginal ($\text{CMF}_{\text{UV}} \approx 0.9$). Cumulonimbus clouds on the other hand, can reduce the UV radiation by more than 80% ($\text{CMF}_{\text{UV}} < 0.2$). Normal medium-high and low clouds have a CMF_{UV} closer to 0.55, i.e 45 % UV irradiance reduction [Koepke et al., 2002].

In general, UV irradiance decreases with increasing cloud amount for all cloud levels. For high clouds, UV irradiance is inversely proportional with solar elevation. The solar elevation dependency for low and medium-high clouds is more complex because its dependency on cloud amount.

Clouds affect UV radiation and global radiation somewhat differently. In one way, the cloud effects are similar: The cloud optical depth, for instance, does not vary considerably with wavelength in the UV and visible range of the spectrum. However, clouds transmit UV radiation more efficiently than global radiation due to strong Rayleigh scattering of photons in the UV range. The difference in cloud attenuation does not only depend on the cloud itself, but also on the solar elevation. The difference is also affected by the fact that clouds absorb radiation in the infrared range, while cloud absorption in the UV and visible range is negligible. Lindfors et al. [2007] developed a method that exploits the differences in cloud attenuation, and converts information on attenuation of global radiation into the UV range, see Section 4.3.

3.5 Transport of Radionuclides: Lagrangian Continuity Equation

To describe the transport of radionuclides through the atmosphere, we can use the continuity equation. The continuity equation can be expressed from a Lagrangian perspective, i.e. coordinates follow the local flow, or an Eulerian perspective, i.e. coordinates are fixed in space. The SNAP model is Lagrangian, and we will therefore present the Lagrangian continuity equation (Eq. 3.3) in this section.

We consider a fluid element located at \mathbf{X}_0 at time t_0 , and we want to know its location after a time t . The *transition probability density*, $P(\mathbf{X}_0, t_0 | \mathbf{X}, t)$, is defined in such a way that the probability the fluid element has moved into a volume (dx, dy, dz) centered around a location \mathbf{X} at time t , is $P(\mathbf{X}_0, t_0 | \mathbf{X}, t) dx dy dz$.

If we let $P(\mathbf{X}, t)$ be the source field for an atmospheric species, and the concentration field at t_0 is $n(\mathbf{X}_0, t_0)$. The concentration field, $n(\mathbf{X}, t)$, is then given as:

$$n(\mathbf{X}, t) = \int_{\text{atm}} P(\mathbf{X}_0, t_0 | \mathbf{X}, t) n(\mathbf{X}_0, t_0) dx_0 dy_0 dz_0 + \int_{\text{atm}} \int_{t_0}^t P(\mathbf{X}', t' | \mathbf{X}, t) P(\mathbf{X}', t') dx' dy' dz' dt' \quad (3.3)$$

The general equation (Eq. 3.3) can be modified to include first-order loss terms, for instance radioactive decay. The SNAP parameterizations of the processes included in the Transition Probability Density 4.1.

3.5.1 Radioactive Decay

During both transportation and deposition, radioactive decay is an ongoing process. The change in radioactivity can be expressed as:

$$N(t + dt) = N(t) e^{-\mu dt}$$

If we let μ represent the decay constant, the half-life $t_{1/2}$, i.e. the time required for the radioactive quantity to be reduced to half of its initial value is:

$$t_{1/2} = \frac{\ln 2}{\mu}$$

We must keep in mind that radioactive decay also affects the amount that has already been deposited on the ground. As mentioned earlier, Cesium-137 has a long half-life of approximately 30 years, and therefore radioactive decay will not affect the concentrations to any significant extent during short term atmospheric transport. However, if we were to look at for instance Iodine-131, a hazardous isotope present in many nuclear reactors, its half-life of 8 days would be important to take into account.

Chapter 4

Methods and Data

4.1 SNAP Model

The SNAP model is a Lagrangian particle model used to simulate atmospheric dispersion after nuclear accidents and nuclear explosions. The atmospheric debris released during the incident is distributed among a large number of abstract model particles. Each model particle therefore carries a given mass of pollutants that can be either gas or particulate matter. The model particles themselves have no physical size and can't be split into smaller parts, but the mass carried by a particle can be subdivided or removed.

The hypothetical nuclear accident we simulate in this thesis, is a nuclear explosion where the concentration of Cesium-137 is released instantaneously and evenly distributed between the model particles. The model particles themselves are evenly distributed within a cylinder-shaped plume with a given height and radius. The model particles will therefore not have the same starting position. If the plume extends above the height of the atmospheric boundary layer (ABL), the transport of particles located above and within the boundary layer will be affected differently by physical processes, see Section 4.1.2.

4.1.1 Weather Scenario

The main input given to the SNAP model for remote application is meteorological data. The meteorological data contains information on the forecasted weather conditions.

Since we are interested in looking at radioactive deposition in Norway, we must let the accident take place during suitable weather conditions. There must be southwesterly winds to make sure the radionuclides are transported in the “wanted” direction. Also, precipitation is a criteria since wet deposition is the most important deposition process for Cesium-137. An additional criteria arises because the motivation behind the thesis is to look at interaction between ionizing and UV radiation: The accident should take place at a time of year when the UV irradiance is not negligible due to low solar elevation.

The time of the scenario is set to 28. August 2015, 18 UTC. The meteorological data provided as input was HIRLAM forecasts [Cucurull et al., 2000] given for 24 hours with a 12 km horizontal grid resolution. At the time of release, there was a low pressure system located south-east of Iceland.

4.1.2 Parameterizations

Height of the ABL

The height of the ABL is calculated by the SNAP model by estimating the Richardson number for each model layer:

$$R_i = \frac{g\Delta\theta_i/\Delta z}{\overline{T}(\Delta\vec{u}/\Delta z)^2} \quad (4.1)$$

$\Delta\theta_i/\Delta z$: gradient of potential temperature

$\Delta\vec{u}/\Delta z$: gradient of the wind speed

g : acceleration of gravity

\overline{T} : Mean temperature of layer

The height of the atmospheric boundary layer is set to the the height of the layer where the Richardson number reaches 1.8: The criteria $R_i = 1.8$ is met.

Advection and diffusion

The advective displacement for each time step is calculated in the SNAP model by using the position of the particle, the forecasted velocity from the numerical prediction model, and the gravitational settling velocity.

$$\vec{x}'_{t+\Delta t} = \vec{x}_t + [\vec{u}(\vec{x}_t) + \vec{u}_g(\vec{x}_t)] \Delta t$$

$\vec{x}_t = \vec{x}(x, y, \eta, t)$: particle position at time t

$\vec{x}_{t+\Delta t} = \vec{x}(x, y, \eta, t + \Delta t)$: intermediate particle position after advection

$\vec{u} = \vec{u}(x, y, \eta, t)$: velocity from the NWP-model

$\vec{u}_g = \vec{u}_g(x, y, \eta, t)$: gravitational settling velocity for given particle

In the SNAP model, diffusion is simulated by using random walk processes. Different values for the parameters are used above and below the ABL. Tests show that diffusion above the ABL is most important for the model results, but in general diffusion is weak and often neglected.

Deposition

Deposition is the process where aerosol particles collect or deposit themselves on the Earth's surface and hence reduce the amount of particles in the atmosphere. Deposition can be divided into two sub-processes: Wet and dry deposition. The rate of the deposition, i.e. the deposition velocity, is slowest for intermediate sized particles. Mechanisms for deposition are most effective for either very small or very large particles. Very large particles are subject to gravitational settling or impaction processes, while very small particles will be influenced by

Brownian diffusion.

Dry Deposition

In the SNAP model, dry deposition only takes place in the surface layer h , which is the lower 10% of the ABL. Above the surface layer, the components are not affected by dry deposition. The Cs-137 that has left the atmosphere by dry deposition and gravitational settling are added to the dry deposition matrix.

In the SNAP model, reduction of mass, m , due to dry deposition is parameterized in the following way:

$$m(t + \Delta t) = m(t) \exp\left(-\frac{v_d}{h_s} \Delta t\right) \quad (4.2)$$

where v_d is the dry deposition velocity and h_s is the height of surface layer.

Wet Deposition

Watersoluble and wettable particles can be deposited through precipitation. Wet deposition can happen in two ways: below-cloud scavenging and in-cloud scavenging. Below-cloud scavenging is when falling rain drops or snow particles collide with aerosol particles through gravitational settling, Brownian diffusion, interception, impaction and/or turbulent diffusion. In-cloud scavenging is when aerosol particles are captured within cloud droplets or cloud ice crystals by functioning as cloud nuclei or through collision.

In the present version of the SNAP model, it is assumed that the mass of the particle, m is reduced by precipitation during one model step in the following way:

$$m(t + \Delta t) = m(t) e^{-k_w \Delta t}$$

The coefficient of wet deposition k_w is according to Baklanov and Sørensen [2001], a function of particle radius r in (μm) and the precipitation intensity q (mm/h).

For below-cloud scavenging, the wet deposition coefficient is calculated differently for three size classes of particles:

$$k_w(r, q) = \begin{cases} a_0 q^{0.79} & r \leq 1.4 \\ (b_0 + b_1 r + b_2 r^2 + b_3^3) f(q) & 1.4 < r \leq 10.0 \\ f(q) & 10.0 < r \end{cases}$$

Wet deposition processes that take place between base and cloud top, depend on the type of precipitation: dynamic or convective. The wet deposition coefficient for dynamic precipitation is similar to the wet deposition coefficient below the cloud base and can be calculated using the equations above.

Wet deposition is more effective for convective precipitation, and is therefore calculated in a different manner. According to Maryon et al., the wet deposition

coefficient for convective precipitation between cloud base and cloud top can be estimated in the following way:

$$k_w(r, q) = a_0 q^{0.79}$$

4.1.3 Input and Assumptions

Cs-137 Concentration:

For our accident scenario, we assume that 1% of the total amount of the HALs stored at Sellafield is released. The total volume of HALs that is stored, is estimated to be 1000 m³, and the concentration of Cs-137 (taking the future multiplication factor 1.5 into account) is estimated to 9420 TBq/m³ [Ytre-Eide et al., 2009]. The amount of released Cs-137 during the scenario is therefore 9.4×10^4 TBq.

Number of Model Particles:

Sensitivity tests indicate that the number of model particles must at least exceed 20 000 [Bartnicki et al., 2011] to avoid large uncertainties, so we let the 9.4×10^4 TBq of Cs-137 be distributed among 100 000 model particles.

Cs-137 Particle Parameters:

The assumed particle size is 2.2 μm .
Particle density is set to 2.3 g/cm³.

Plume Dimensions:

The height of the ABL at the time of the scenario (28. August 2015) was estimated by the SNAP model to be 1013 m at the location of Sellafield. The SNAP model was run for the following plume heights: 800 m, 1100 m and 2000 m. The height of the plume in relation to the height of the ABL determines how the different processes which affect transport come into play. We have therefore selected a plume height within the boundary layer, height that just exceeds the ABL height and lastly a height that greatly exceeds the height of the ABL. The radius of the plume was set to 100 m.

4.2 The libRadtran Package

To calculate the UV irradiance at the selected weather stations in the deposition area, the libRadtran package is used. The libRadtran (Library of Radiative Transfer) package is a collection of functions and programs for calculating the transfer of solar radiation in the Earth’s atmosphere [Mayer et al., 2012]. Within this package, there is a wide selection of solvers available for solving the RTE (Eq. 3.2) and the state of the atmosphere can be determined in detail. Our choice of solver and input parameters will be described in the sections below.

4.2.1 Disort Solver

When running libRadtran, the disort solver is applied [Stamnes et al., 2000]. This solver uses the Discrete Ordinate Method where the the integral over all incoming directions on the right hand side in RTE, is replaced by a sum over discrete directions. The radiances from the different directions are weighted differently to give a approximation of the actual radiance. The directions in the approximation are called streams, and the number of streams can be chosen by the user. A high number of streams will give a more accurate answer, but will also increase the computing time. The number of streams was set to 6 in our simulations.

4.2.2 Input and Assumptions

Number of Vertical Layers:

In our simulations, the atmosphere is divided into 50 vertical layers. The RTE is solved for each layer seperately. The radiance in the surrounding layers are used as continuity conditions, while the radiance at the top of the atmosphere and at the surface are boundary conditions. The optical thickness and phase function can be determined for each layer seperately, see Fig. 4.1.

Asymmtery Factor:

The asymmtery factor describes how forward-peaked the scattering is. When the phase function is not known, it can be set to be the Henyey-Greenstein phase function, Eq. 4.3. This phase function is not physical, but works well for most cases and is easy to use since it’s only dependent on the asymmetry factor: g . The aerosol asymmtery factors are given by the Shettle [1990] aerosol model.

$$p(\theta) = \frac{1}{4\pi} \frac{1 - g^2}{[1 + g^2 - 2g \cos \theta]^{3/2}} \quad (4.3)$$

Plan Parallel or Spherical Atmosphere:

For zenith angles larger than 82° , the difference in distance under the assumption of a plan-parallel atmosphere compared to the actual path can give large errors. Since we are calculating daily UV doses, we need to integrate over the entire span of daylight hours, i.e. all solar zenith angles between 0 and 90° –

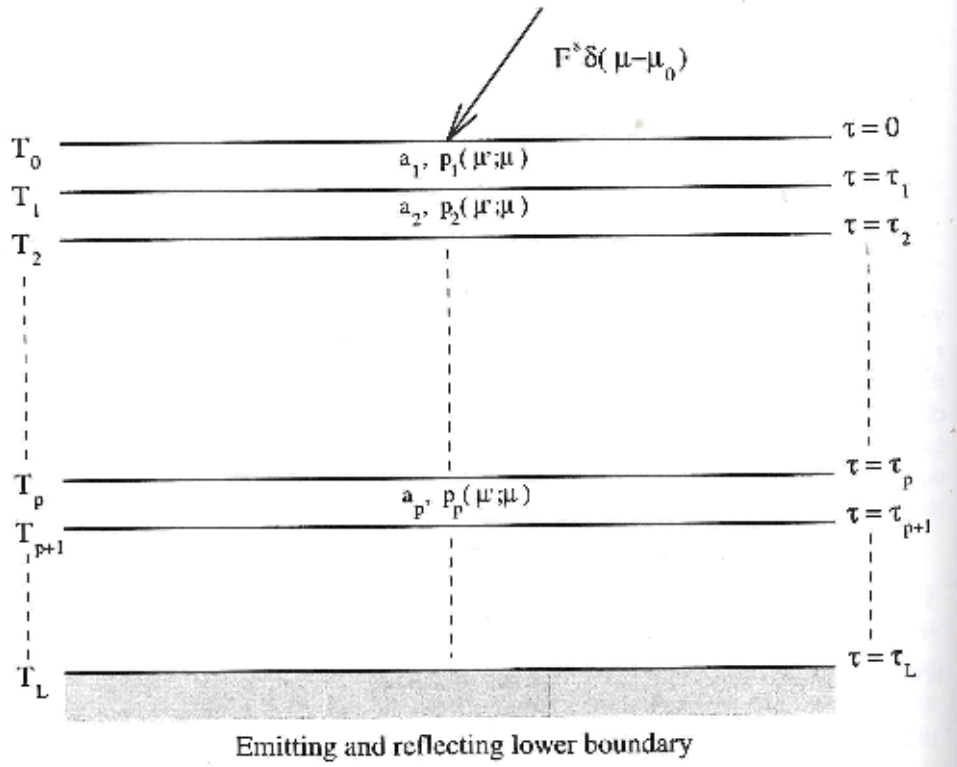


Figure 4.1: Schematic illustration of multilayered medium. T , τ , a and p signify temperature, optical depth, single-scattering albedo and phase function respectively. $F^S \delta(\mu - \mu_0)$ represents the incoming solar radiation [Thomas and Stamnes, 2002].

pseudospherical must therefore be turned on.

Gas Absorption Parameterization:

Gas absorption parameterization is set to kato2 for the global radiation runs. The absorption lines are approximated by band parameterization. The tables are an optimized version (157 subbands) of the original kato method [Kato et al., 1999].

Aerosols:

`aerosol_default` sets up the aerosol model by Shettle [1990]. The default settings are rural type aerosols in the boundary layer, background aerosols above 2 km, spring-summer conditions and a visibility of 50 km. They assume a mixture of water soluble and dust-like aerosols. As mentioned, the Shettle [1990] model determines the aerosol asymmetry factor. The wavelength dependence of the aerosol optical depth (AOD) is accounted for by Ångström parameterization

(Eq. 4.4). We have adjusted the Ångström-parameters: α is set to 1.1, and β is set to 0.06 for the end of August and September according to Lindfors et al. [2007].

$$\text{AOD}_\lambda = \beta \lambda^{-\alpha} \quad (4.4)$$

Delta-m Scaling On/Off:

The phase function for forward-peaked scattering in the RTE is complicated and needs to be represented by hundreds of terms. Instead of using the complete phase function in these cases, the δ -m method is implemented. In this scaling method, photons scattered within small angles of the forward peak are not scattered at all. The “direct flux” will therefore contain scattered beams, resulting in a scaled optical depth $\hat{\tau}$ which is smaller than the original τ . Also, the absorption is artificially increased, $\hat{a} > a$. Delta-m scaling is turned on.

Atmospheric Profile:

The atmosphere file contains the following information:

- Altitude above sea level in km
- Pressure profile in hPa
- Air density profile in molecules/cm⁻³
- Ozone density profile in molecules/cm⁻³
- Oxygen density profile in molecules/cm⁻³

We’ve used the AFGL atmosphere profile for midlatitude summer [Anderson et al., 1986]. Water vapour column is scaled to match the daily values retrieved from the ERA-Interim reanalysis dataset [Dee et al., 2011]. The ozone layer concentrations were scaled with ozone data retrieved from Bjørn Johnsen (NRPA). The ozone data were based on daily gridded data from OMI/AURA, version L3.

Solar Flux:

The solar flux at the top of the atmosphere is set in compliance to the kato method [Kato et al., 1999] when performing libRadtran runs for global radiation. For the UV simulations, the solar flux was set to the `atlas_plus_modtran` file which combines features of the extraterrestrial spectrum from ATLAS3, ATLAS2 and MODTRAN [Mayer et al., 2012].

4.3 Clouds: The Lindfors Method

To be able to apply information on cloud attenuation of global radiation in the UV range, Lindfors et al. [2007] developed a look-up table by running libRadtran for clear sky conditions and comparing with runs where a cloud layer was implemented. The CMF_{UV} values presented in their table, are for erythemally-weighted UV. The same principle may be applied to develop look-up tables for other action spectra, for instance the action spectrum for DNA damage.

The Lindfors method consists of three steps:

- 1) Simulating clear-sky irradiances for global radiation (G_{clear}) and UV radiation (UV_{clear}) with libRadtran.
- 2) Using the measured irradiance ($G_{\text{all-sky}}$) and simulated clear-sky irradiance (G_{clear}) for global radiation to determine CMF_G according to $\frac{G_{\text{all-sky}}}{G_{\text{clear}}}$ and finding the corresponding CMF_{UV} in a look-up table.
- 3) Use the given information to calculate the reconstructed UV irradiance according to:

$$\text{UV}_{\text{reco}} = \text{UV}_{\text{clear}} \cdot \text{CMF}_{\text{UV}} \quad (4.5)$$

The dependency of CMF_{UV} on CMF_G for different zenith angles, is given in Fig. 4.2.

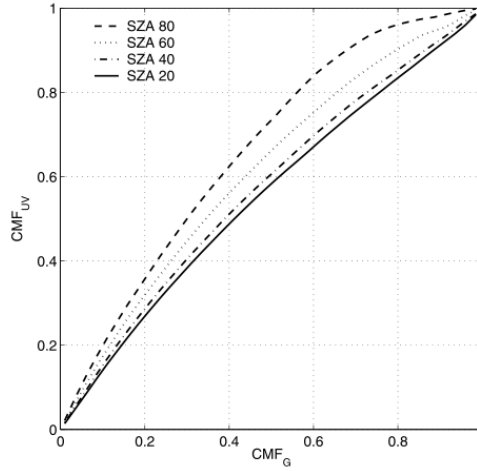


Figure 4.2: The dependence of CMF_{UV} on CMF_G for different zenith angles [Lindfors et al., 2007].

4.3.1 Global Radiation Data

Global radiation is measured by horizontally mounted pyranometers. Hourly means of global radiation, are available at several stations in Western Norway. In this thesis, we have selected three stations, see Table 4.1 and Fig. 4.3. In order to find the CMF_{UV} to account for cloud effects in the UV range, we must first calculate the CMF_{G} using the available global radiation values.

Table 4.1: Selected Stations with Hourly Global Radiation Data

Station	County	Coordinates (°N, °Ø)
Fureneset	Sogn og Fjordane	61.2928, 5.0443
Flesland (Bergen)	Hordaland	60.2892, 5.2265
Særheim	Rogaland	58.7605, 5.6505

Since the measured global radiation data are given as means over the last hour, we ran libRadtran with a time step of one hour, letting the solar zenith angle in the middle of the time period represent the mean value.



Figure 4.3: Stations with available global radiation data indicated with red dots. With descending latitude: Fureneset, Flesland and Særheim.

Chapter 5

Results

We will first present the results from running SNAP model for a Sellafield accident set to 28 August 2015 18 UTC in Sections 5.1-5.4. Afterwards, the time development of the deposition at the selected stations will be briefly described.

In Section 5.6, the daily total Standard Erythema Dose (SED) will be presented for the three stations in the month after Cs-137 deposition (29. August - 29. September 2015). The clouds' effect on the hourly UVI maximum for each day will be presented in Section 5.7, before the time development of UVI for selected days is shown in more detail in Section 5.8.

The Lindfors method is briefly validated in Section 5.9 using global radiation for Bergen (Florida). In Fig. 5.11, the Daily SED for the Florida simulations and measurements are shown.

5.1 Cs-137 Accumulated Wet Desposition

The accumulated wet deposition of Cs-137 after 48 hours for different plume heights, is shown in Fig. 5.1. The wet deposition associated with a plume height of 800 m, seems to be concentrated along a weather front associated with the low pressure south-east of Iceland.

For plume heights extending the ABL, the wet deposition is more widespread indicating that particles released at these heights, are wet deposited by other means than precipitation associated with weather front.

5.2 Cs-137 Accumulated Dry Desposition

The accumulated dry deposition of Cs-137 after 48 hours for different plume heights, is shown in Fig. 5.2. As expected, since only Cs-137 particles in the surface layer can be dry deposited, the extent of dry deposition is reduced with increasing plume height. Most of the Cs-137 is dry deposited in the Atlantic

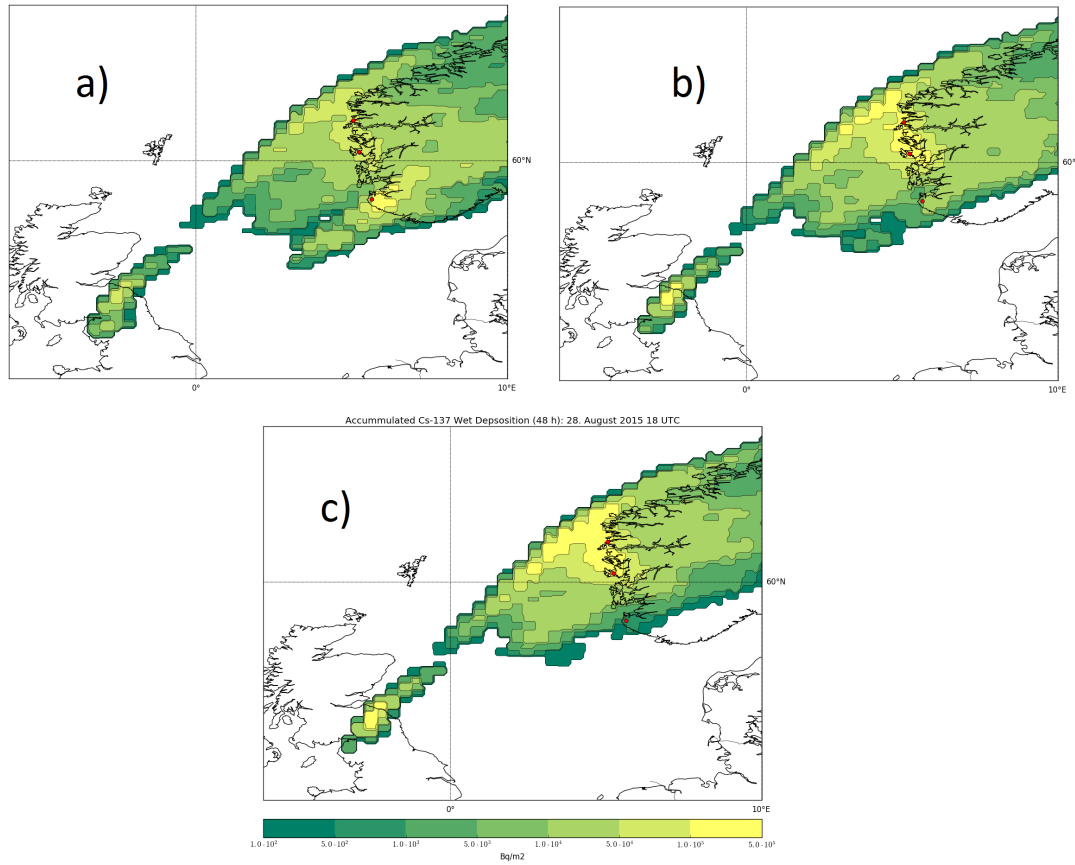


Figure 5.1: Accumulated wet deposition of Cs-137 after 48 h for plume height a) 2000 m, b) 1100 m and c) 800 m. The red dots indicate the weather stations. The range is from 10^2 to $5.0 \cdot 10^5$ Bq/m².

Ocean before reaching Norway.

5.3 Cs-137 Deposition for Selected Stations

The accumulated Cs-137 concentrations due wet deposition, dry deposition and total deposition are presented in Tables 5.1-5.3.

The accumulated wet deposition at Fureneset decreases with increasing plume height. For Flesland, the highest plume height also gives the smallest wet deposition value. However, the wet deposition is slightly higher for a plume height of 1100 m than 800 m. For Særheim, there is a drastic increase in wet deposition when the plume height increases. For a plume height of 800 m, hardly any Cs-137 is wet deposited at Særheim (597 Bq/m^2), while for a plume extending

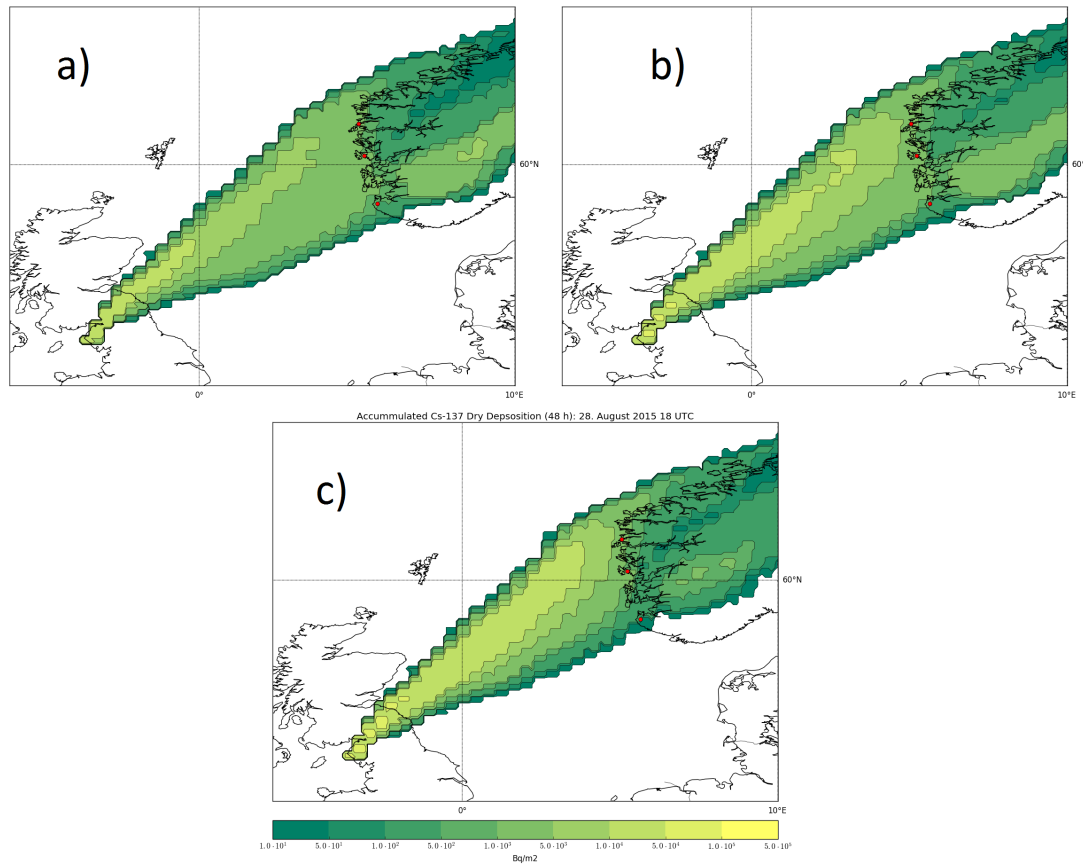


Figure 5.2: Accumulated dry deposition of Cs-137 after 48 h for plume height a) 2000 m, b) 1100 m and c) 800 m. The red dots indicate the weather stations. The range is from 10 to $5.0 \cdot 10^5$ Bq/m²

far beyond the ABL, the wet deposition is $1.76 \cdot 10^5$ Bq/m².

According to the contamination levels presented in The Nordic guidelines for nuclear accidents [NRPA, 2014], areas with concentrations of strong β - or γ -emitters in the range $10^5 - 10^6$ Bq/m² are deemed *contaminated*. The weather stations Fureneset and Fureneset become contaminated for plume heights 800 and 1100 m due to total deposited Cs-137 concentrations exceeding 10^5 Bq/m². Særheim weather station reaches the contaminated level for a plume height of 2000 m.

Table 5.1: Accumulated wet deposition of Cs-137 [Bq/m²]

Plume height	Fureneset	Flesland	Særheim
800 m	$1.31 \cdot 10^5$	$1.04 \cdot 10^5$	$5.97 \cdot 10^2$
1100 m	$1.11 \cdot 10^5$	$1.18 \cdot 10^5$	$1.07 \cdot 10^4$
2000 m	$6.18 \cdot 10^4$	$7.17 \cdot 10^4$	$1.76 \cdot 10^5$

Table 5.2: Accumulated dry deposition of Cs-137 [Bq/m²]

Plume height	Fureneset	Flesland	Særheim
800 m	$2.27 \cdot 10^3$	$1.02 \cdot 10^3$	$3.69 \cdot 10$
1100 m	$2.70 \cdot 10^3$	$1.83 \cdot 10^3$	$3.04 \cdot 10^2$
2000 m	$1.54 \cdot 10^3$	$1.16 \cdot 10^3$	$3.87 \cdot 10^2$

5.4 Sum of Cs-137 Deposition For Selected Stations

The deposited Cs-137 concentration sums for all three stations, can be found in Table 5.4-5.6.

For our weather scenario, the accumulated wet deposition sum for the three stations Fureneset, Flesland and Særheim is greatest when we let the height of the explosion plume extend to 2000 m. Wet deposition being the dominant deposition process, a plume height of 2000 m will also give the highest total accumulated deposition. For lower plume heights, a greater portion of the Cs-137 is deposited in the ocean, instead of over land.

Dry deposition only affects particles within the surface layer and therefore the lowest sum can be seen for the highest plume height. The sum of accumulated dry deposition at the selected weather stations for the selected weather scenario, is greatest when the plume extends above the initial boundary layer, increasing the likelihood of long-range transport for some particles. However, the particles are still “within reach” of the boundary layer, so that the particles can be dry deposited at a later time.

5.5 Time Development of Deposition

5.5.1 Fureneset

For all heights at Fureneset station, the deposition first occurs as wet deposition in the time period 12-15 hours after the explosion. All the Cs-137 at this station is deposited within 18 hours after the accident.

5.5.2 Flesland

Flesland first experiences both dry and wet deposition in the period 12-15 hours after the explosion. All Cs-137 deposition happens within 18 hours.

Table 5.3: Total accumulated deposition of Cs-137 [Bq/m²]

Plume height	Fureneset	Flesland	Særheim
800 m	$1.34 \cdot 10^5$	$1.05 \cdot 10^5$	$6.36 \cdot 10^2$
1100 m	$1.14 \cdot 10^5$	$1.20 \cdot 10^5$	$1.10 \cdot 10^4$
2000 m	$6.33 \cdot 10^4$	$7.29 \cdot 10^4$	$1.76 \cdot 10^5$

Table 5.4: Wet accumulated deposition of Cs-137 [Bq/m²]

Plume height	Deposition Sum
800 m	$2.36 \cdot 10^5$
1100 m	$2.40 \cdot 10^5$
2000 m	$3.09 \cdot 10^5$

5.5.3 Særheim

At Særheim, both wet and dry deposition first occur in the period 9-12 hours after the accident. All Cs-137 deposition happens within 15 hours.

The described time of the Cs-137 deposition development is the same for all plume heights.

Since all the deposition at the three weather stations takes place before 29. August 2015 12 UTC, we modelled UV irradiances with libRadtran for 29. August 2015 and the following month.

5.6 Daily UV Dose (SED) After Deposition

Fig. 5.3 shows how the daily SED is reduced by cloud cover for the three stations in the period after the hypothetical Cs-137 fallout. For clear sky conditions, the daily SED is overall determined by the solar elevation, and will therefore decrease with increasing day number. The daily variations in SED for clear skies are caused by changes in water vapour column and ozone column.

Comparing the clear sky values (blue curve) with values when clouds are accounted for (green curve), we see that cloud cover can attenuate the erythemal dose significantly and give large day to day variations. The potential SED is determined by day number, but the actual SED is strongly dependent on the presence of clouds.

5.7 Cloud Effects on UVI Maximum

For clear skies, the pattern of daily maximum UVI per hour is distinct for the three stations: the lowest latitude, i.e the highest solar elevations determines

Table 5.5: Dry accumulated depositions [Bq/m²]

Plume height	Deposition Sum
800 m	$3.62 \cdot 10^3$
1100 m	$4.84 \cdot 10^3$
2000 m	$3.09 \cdot 10^3$

Table 5.6: Total accumulated deposition [Bq/m²]

Plume height	Deposition Sum
800 m	$2.39 \cdot 10^5$
1100 m	$2.45 \cdot 10^5$
2000 m	$3.12 \cdot 10^5$

which station has the highest UVI value. In our case, this is Særheim weather station, located at 58.7605 °N.

The pattern when clouds are accounted for in the model is more unclear. Although the greatest solar elevation has a tendency to result in the greatest UVI maximum, the order is not necessarily determined by latitude. This can be seen for September 1. September (day 244), when the order of the stations is reversed: the UVI maximum is greatest for Fureneset, followed by Flesland and Særheim. Differences in cloud cover may also result in large differences in UVI between the stations. For 2. September (day 245), the expected maximum UVI for clear sky conditions are between ~ 3 and 3.5 for all three stations. When clouds are accounted for, the span in UVI is from ~ 1 to 3 .

As mentioned in Section 3.2, protective measures are recommended when UVI exceeds 2. UVIs below 2 are deemed harmless: The received UV doses are too small to produce sunburn. UVIs between 2 and 3 are in the lower part of moderate range, and may cause erythema if a fair-skinned person is out in the sun over time. In practice, only UVIs that exceed 3 are deemed potentially harmful. As we see from Fig. 5.4, only 30. August - 9. September (Day 245-252) have UVI values that exceed 3.

Other health effects on humans and effects on the environment may have different dose-effect relationships. These will not be discussed further in this thesis, but the same tools can be used, adjusted for various action spectra of UV and possibly relative biological efficiency (w_T weighting factors) of ionizing radiation.

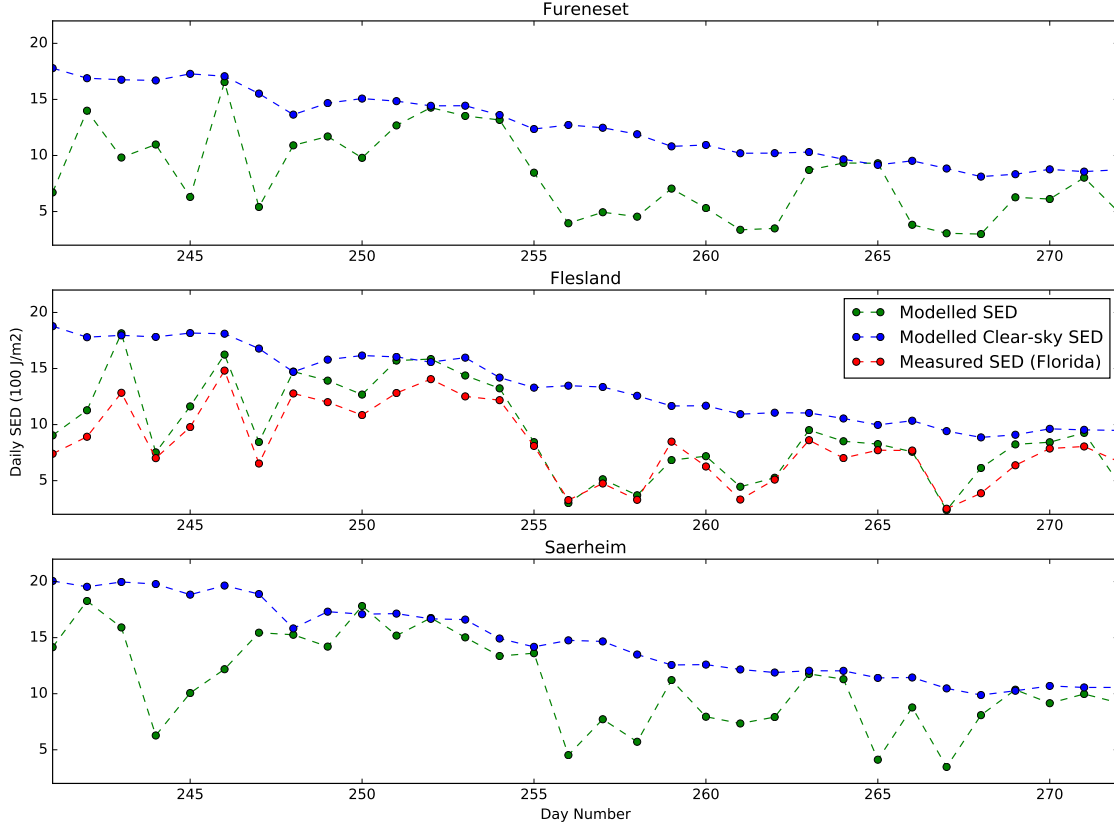


Figure 5.3: Total Daily SED for 29. August - 29. September 2015

5.8 UV Index at Fureneset, Flesland and Særheim for Selected Days

The UVI index for the selected days are shown in Fig. B.32-Fig.5.10. The measured UVI presented is given as minute values from a GUV instrument at Florida, Bergen (60.3833 °N, 5.3333 °E). There is a distance of ~ 12 km between the stations Flesland and Florida.

The spiky shape of the measurement curve demonstrated in Fig. B.32, illustrates the nature of clouds: The presence of clouds varies significantly with time and space. A passing cloud can attenuate UV radiation at a given time, and once it has passed, cloud free conditions are again obtained.

As mentioned in Section 3.4.5, if the solar disk is visible, clouds can enhance the UV irradiance. In Fig. 5.8 and Fig. 5.9, the modelled values for cloudy conditions exceed the ones for clear sky conditions, due to a calculated CMF_{UV}

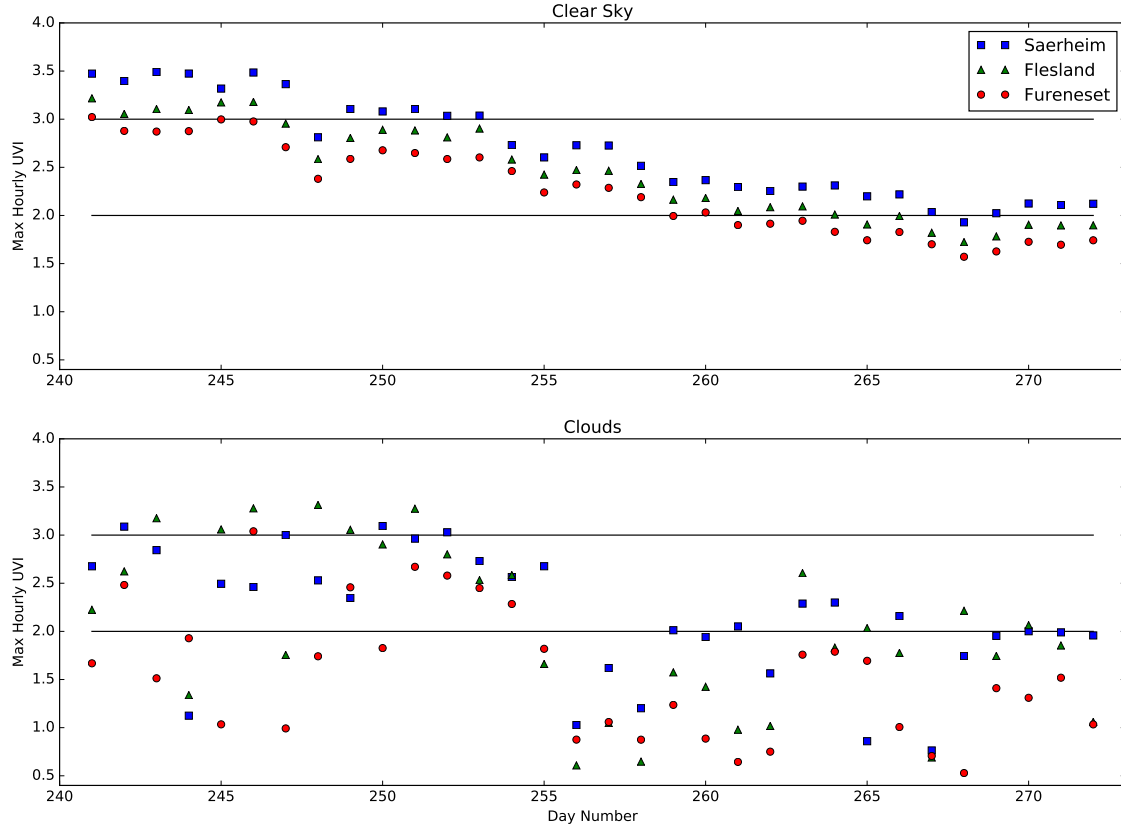


Figure 5.4: Pattern of daily UVI maximum per hour for modelled clear skies and cloudy conditions

above 1. Cloud cover data from eklima/met.no are only reported every hour, and we have run the model 30 minutes before and after these observations are made. However, the available cloud cover information does not exclude that enhancement is possible.

2. September (Fig. 5.6) illustrates how a change in cloud cover may affect UVI throughout the day for a single station. For Flesland station the conditions are first overcast, before the cloud cover is dissolved and clear sky conditions occur. The plot for 2. September also demonstrates that the time development may differ between locations: While the conditions are overcast for the entire span of the day at Fureneset, Flesland experiences a shift from cloud cover to clear sky. Særheim experiences a brief period of clear sky conditions before the conditions become cloudy again.

As we can see from Fig. 5.7, 9. September represents a day with clear sky

conditions for all three stations, and can therefore indicate how well libRadtran simulates UV irradiance in general by comparing the output for Flesland with the measurements from Florida, Bergen. The model slightly overshoots the UVI in the middle of the day. In our model, we have not given accurate aerosol information, only set up the default aerosol model. For the same day, the blue and red curves overlap for Fureneset and Særheim – CMF_{UV} is equal to 1. This reflects that the model runs and the measured means of global radiation correspond well for clear sky conditions at these stations.

In general, the UVI for Flesland and Florida seem to correspond quite well. However, and clouds effects can be extremely local. This can be seen in Fig. 5.10. The green curve for measurements at Florida indicates clear sky conditions in the beginning of the day, while the red curve for the model run at Flesland, indicates cloud attenuation. Using cloud cover data from eklima/met.no, we see that the conditions at Flesland are completely overcast at this period of the day for the given date, 29. September 2015. The conditions at Florida however, indicate clear skies.

Fig. A.12 represents a day with overcast conditions (8 octas) for the entire span of day at Flesland. The UVI plots show that the UV radiation is significantly attenuated during these conditions. However, cloud cover doesn't give any information on what type of clouds are present. The cloud attenuation for an entire overcast day may vary depending on what kind of clouds are present.

The rest of the daily plots are available in Appendix A.

Looking at the UVI plots for the separate days, Flesland seems to have more enhancement than Særheim and Fureneset. At least, for certain periods the measured global radiation at Flesland exceeds the modelled global radiation for clear skies. This enhancement is not seen for the daily UVI plots for Florida in Appendix B, and therefore may be due to local cloud effects.

5.9 Performance of Lindfors Method

Our choice of weather stations for this master project, was based on which stations had available global radiation data at eklima.met.no. For validation purposes, global radiation data for Florida was retrieved from the webpage “Weather in Bergen” (veret.gfi.uib.no).

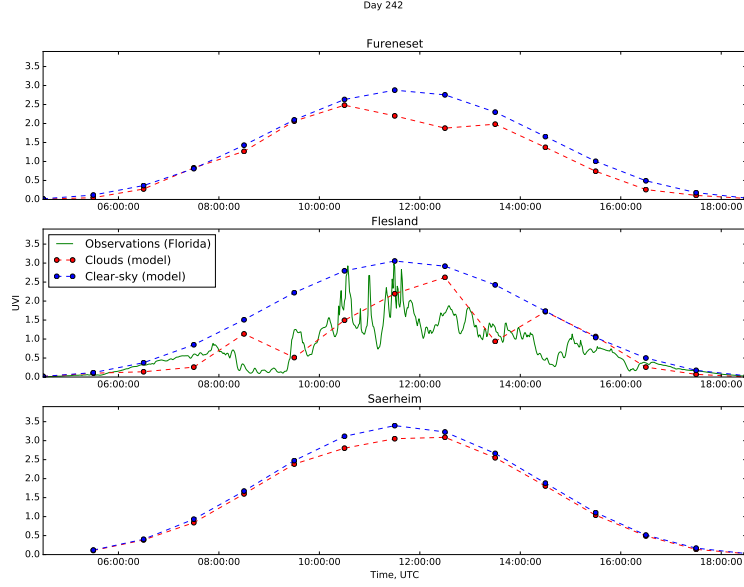


Figure 5.5: Calculated UV Index for 30. August 2015.

Daily UVI plots for Florida can be found in Appendix B.

Overall, the simulations using the Lindfors method are able to capture the tendencies in UVI through the span of the day. However, the global radiation data for 20. September and 21. September seem to be interchanged (Fig. B.23-B.24). As we can see from Fig. B.21, there can be large variations in measured UVI over short time spans. Running libRadtran with a time step of one hour, cannot reproduce these variations.

The Root-Mean-Square (RMS) error is given as:

$$\text{RMS}(\%) = \sqrt{\frac{1}{n} \sum_{i=1}^n \left(\frac{E_i - R_i}{R_i} \right)^2} \cdot 100\% \quad (5.1)$$

The RMS error for the daily SED calculated with the Lindfors Method for 29. August - 29. September 2015, is 15.35%. Removing 20. and 21. September, the RMS error is reduced to 13.11%. It should be noted that our model is run for a short time period. The method is expected to perform better on a larger time scale, capturing the general trend in erythemal UV irradiance.

The differences between measurements and simulations of daily SED, are given in Fig. 5.11. The difference in daily SED is greatest for 20. september (day 263) – when the assumed interchange is not corrected for. The figures in Appendix B indicate that the differences in measured and calculated daily SED is due to large variations in UV irradiance over short time spans.

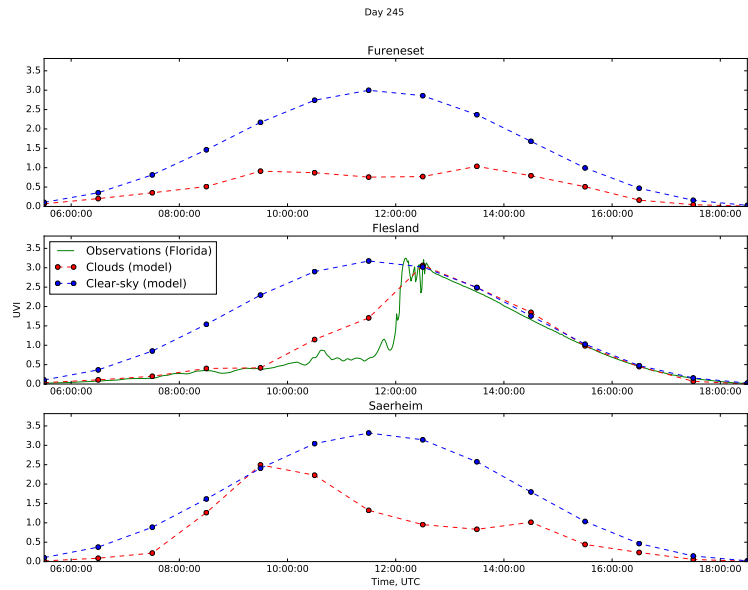


Figure 5.6: Calculated UV Index for 2. September 2015

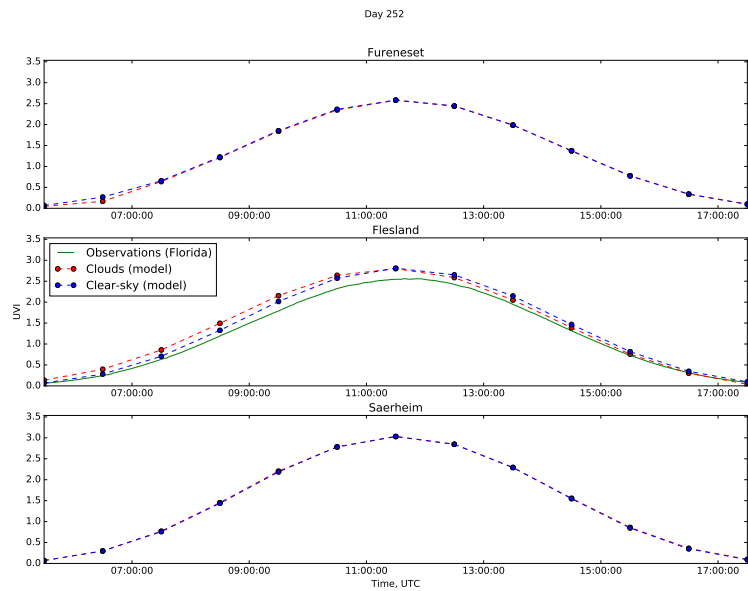


Figure 5.7: Calculated UV Index for 9. September 2015

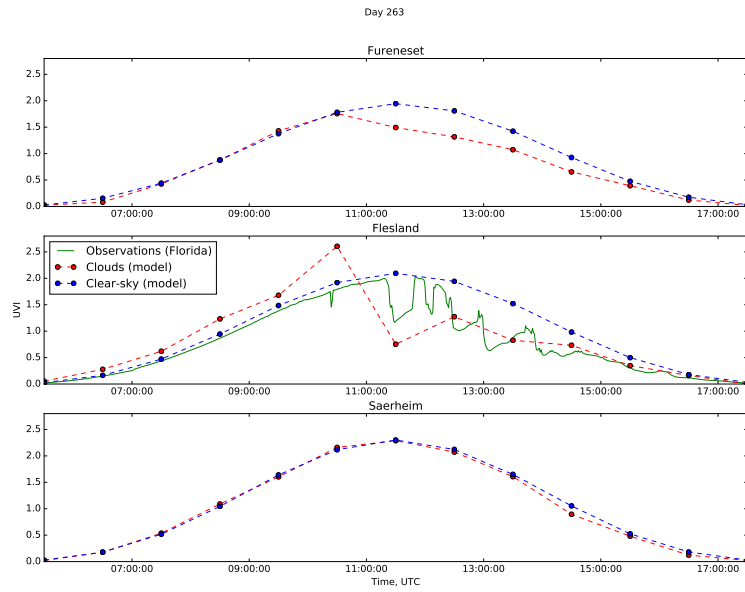


Figure 5.8: Calculated UV Index for 20. September 2015

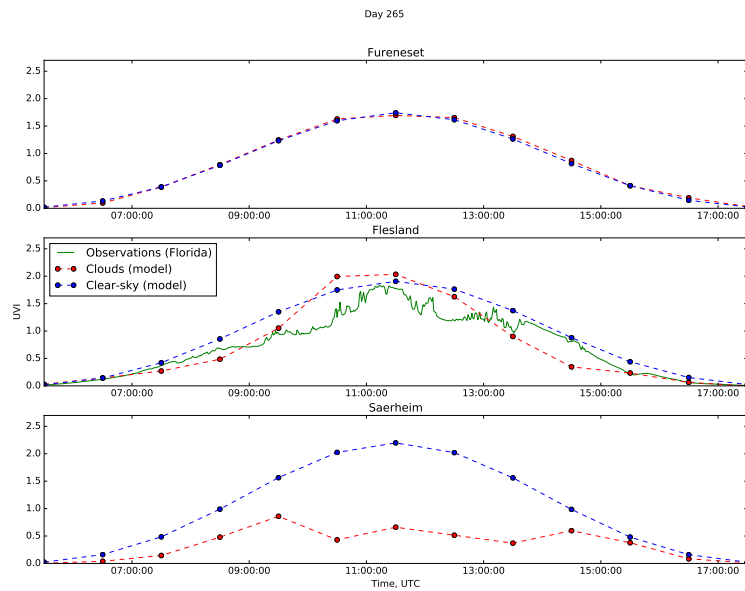


Figure 5.9: Calculated UV Index for 22. September 2015

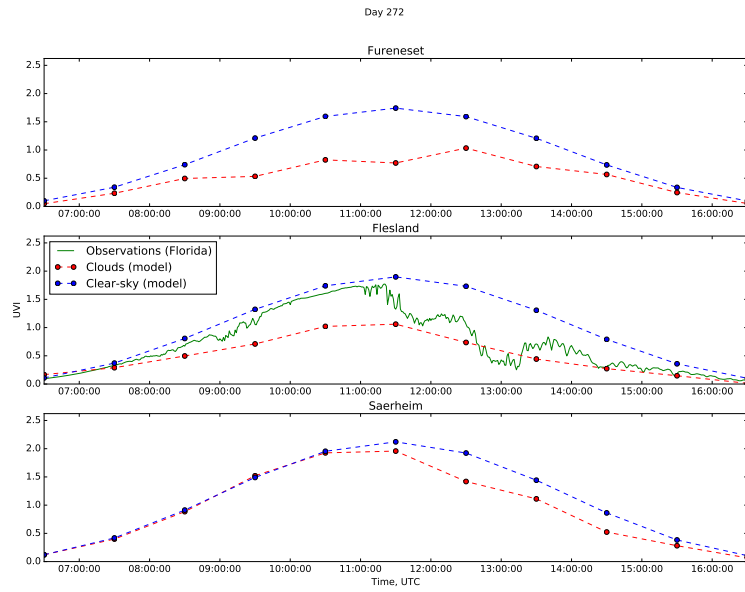


Figure 5.10: Calculated UV Index for 29. September 2015

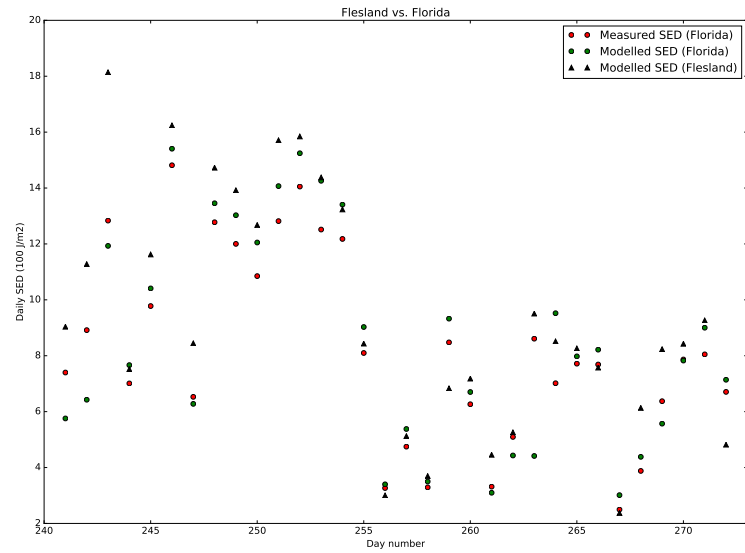


Figure 5.11: Daily SED for Florida. Calculations for Flesland are also included.

Chapter 6

Discussion and Future Perspectives

The aim of this thesis is to investigate the effect the state of the atmosphere has on transport of radionuclides and UV transfer in relation to a nuclear accident. An overall goal is to be able determine how additional exposure of ionizing radiation affects the health consequences of daily UV exposure. Investigating transfer and transport we've done in this thesis, is the first step to reaching this goal.

The weather conditions at the time of release of Cs-137, were crucial in determining the impact of the nuclear accident. During experiments with the SNAP model, the nuclear explosion was set 27. August 2015 12 UTC. For this scenario, no wet deposition would occur in Norway. Instead of being wet deposited in Western Norway, the Cs-137 reached Sweden and Denmark.

By plotting deposition maps for different plume heights, it becomes evident that the plume height has great impact on how much is deposited at the different weather stations. The effect of plume height was especially significant at Sørheim station. Even though the deposition occurred in the same time periods for all plume heights, the amount of deposited Cs-137 differed with many orders of magnitude: from $\sim 500 \text{ Bq/m}^2$ for a plume of height of 800 m to $\sim 10^5 \text{ Bq/m}^2$ for a plume height of 2000 m – a concentration of Cs-137 which fulfills the criteria for *contamination* according to the Nordic guidelines [NRPA, 2014].

If a nuclear accident were to happen, it is therefore not only important to have a forecast that predicts the future weather conditions accurately to provide the SNAP model with input: Knowing the plume geometry is also crucial for how well SNAP can predict the fallout.

libRadtran is a 1D radiative transfer model and hence provides UV irradiance for a given location. The SNAP model gives deposition fields as output. Preferably, libRadtran output values could be interpolated to produce UV maps. Then the UV irradiance fields could be compared to the deposition fields to in-

investigate possible interaction. Martin Album Ytre-Eide at NRPA is currently working on producing UV maps that take variations in elevation and albedo into account.

It must be noted that the operational SNAP model is offline: Even though it uses real-time weather forecasts, the forecasts are not affected by the released radionuclides. Being watersoluble, Cs-137 may serve as cloud condensation nuclei (CCN) or affect other CCN through ionizing radiation. Wet deposition is the most important deposition process for Cs-137, and therefore changes in CCNs, cloud formation and precipitation pattern will affect the deposition pattern as well. A change in the presence of clouds, will also have an impact on the UV irradiance reaching the surface. As the figures in Section 5.8 demonstrated, the UV irradiance is greatly dependent on cloud cover.

The plot over hourly max UVI (Fig. 5.4) showed that only the first days after deposition had UV irradiances capable of producing UV erythema. The interaction between UV and ionizing radiation is not determined, so we do not know how the ionizing radiation doses from the deposited Cs-137 may affect the risk for UV damage. However, as Leenhouts and Chadwick described in their analysis, synergism is a possibility, and DNA damage may therefore occur for lower UV irradiances when being exposed to ionizing radiation simultaneously.

With Leenhouts' and Chadwick's synergistic model in mind, it would be more appropriate to weight the modelled UV irradiances with the action spectrum for DNA damage, instead of the action spectrum for erythema. However, the method used for reconstructing UV irradiance for the time period after the hypothetical fallout, was developed for erythema UV doses. Lindfors et al. suggested that their method could be adjusted to account for other action spectra. For our cause it would be preferable with a modified look-up table with CMF_{UVS} accounting for DNA damage.

There are a significant number of ways for an individual to be exposed to ionizing radiation after a nuclear accident. Direct exposure and uptake of radionuclides through inhalation and skin contamination, are the most direct pathways. Indirect pathways, include ingesting foodproducts containing radioactive components. Plant tissue may absorb radionuclides directly if they are deposited on the plant itself. The radionuclides may be integrated in the soil and transported to the edible parts of the plant by root uptake. Grazing animals may eat plants containing radionuclides, resulting in radioactive meat and milk products. The numerous amount of pathways for ionizing radiation exposure is beyond the scope of this thesis, but the results presented may serve as a starting block for dose calculations for the pathways of interest.

In this thesis, we focused on UV doses in the time period shortly after the deposition of Cs-137: September 2015. In October 2015 and the following months, the solar elevation will be reduced and UV irradiance will become negligible in winter. However, it must be kept in mind that Cs-137 is a long-lived radionuclide and the pathways into foodproducts may be slow processes. The interaction between the two radiative components in organisms related to a nuclear accident is therefore not limited to the time directly after deposition – it

will be present the following spring and in the years to come. 30 years after, the Chernobyl disaster still costs the Norwegian government 15 millioner NOK annually in countermeasurements to limit harmful contamination. Norway is better prepared for a nuclear accident today than in 1986, but the clean-up after a nuclear accident is an extensive and time-consuming task.

It is also important to emphasize that exposure to UV radiation and ionizing radiation are not events that occur once – radiative exposure happens on a basis. The duration of the exposure and the number of exposure events may vary from day to day depending on our behaviour and surroundings. The risk of developing cancer due to radiative exposure is accumulative: The more exposure, the greater the risk. When describing the interaction between UV and ionizing radiation in Section 2.6, we referred to lab experiments where consequences of combining two separate exposures were investigated. However, considering that radiative exposure is a reoccurring event and the accumulative nature of the effects, it would be desirable to determine how UV and ionizing radiation affect each other in the long run by comparing life-time doses and determining whether there is an increased risk of developing, for instance, skin cancer.

References

- G. P. Anderson, S. Clough, F. Kneizys, J. Chetwynd, and E. P. Shettle. Afl at-
mospheric constituent profiles (0.120 km). Technical report, DTIC Document,
1986.
- A. Baklanov and J. Sørensen. Parameterisation of radionuclide deposition in
atmospheric long-range transport modelling. *Physics and Chemistry of the
Earth, Part B: Hydrology, Oceans and Atmosphere*, 26(10):787–799, 2001.
- J. Bartnicki, H. Haakenstad, and Ø. Hov. Operational snap model for remote
applications from nrpa. Technical report, met.no, 12 2011.
- J. Calbo, J.-A. González, et al. Empirical studies of cloud effects on uv radiation:
A review. *Reviews of Geophysics*, 43(2), 2005.
- Cancer Registry of Norway. Cancer in norway 2013 - cancer incidence, mortality,
survival and prevalence in norway. Special issue / Spesialnummer: Krefte i
Norges fylker 1954–2013, 2015.
- T. Cook, Z. Wang, S. Alber, K. Liu, S. C. Watkins, Y. Vodovotz, T. R. Billiar,
and D. Blumberg. Nitric oxide and ionizing radiation synergistically promote
apoptosis and growth inhibition of cancer by activating p53. *Cancer Research*,
64(21):8015–8021, 2004.
- L. Cucurull, B. Navascues, G. Ruffini, P. Elosegui, A. Rius, and J. Vila. The use
of gps to validate nwp systems: the hirlam model. *Journal of Atmospheric
and Oceanic Technology*, 17(6):773–787, 2000.
- D. Dee, S. Uppala, A. Simmons, P. Berrisford, P. Poli, S. Kobayashi, U. Andrae,
M. Balmaseda, G. Balsamo, P. Bauer, et al. The era-interim reanalysis:
Configuration and performance of the data assimilation system. *Quarterly
Journal of the royal meteorological society*, 137(656):553–597, 2011.
- J. G. Estupiñán, S. Raman, G. H. Crescenti, J. J. Streicher, and W. F. Barnard.
Effects of clouds and haze on uv-b radiation. *Journal of Geophysical Research:
Atmospheres*, 101(D11):16807–16816, 1996.
- U. Feister and R. Grewe. Spectral albedo measurements in the uv and visible
region over different types of surfaces. *Photochemistry and Photobiology*, 62
(4):736–744, 1995.
- geigercounter.org. Cs-137 decay, 2017. URL [http://www.geigercounter.org/
radioactivity/cesium-137-decay.gif](http://www.geigercounter.org/radioactivity/cesium-137-decay.gif). [Online; accessed March 09, 2017].

- O. Harbitz and L. Skuterud. *Radioaktiv forurensing – betydning for landbruk, miljø og befolkning*. Landbruksforlaget, Landbruksforlaget AS, Postboks 9303, Grønland, 0135 Oslo, 1 edition, 1999. ISBN 8252921973. An optional note.
- I. INES. The international nuclear and radiological event scale user’s manual 2008 edition. *IAEA and OECD/NEA*, 2008.
- M. Iqbal. *An introduction to solar radiation*. Elsevier, 2012.
- B. Johnsen, T. Christensen, L. T. Nilsen, and M. Hannevik. Ultraviolet radiation, sun damage and preventing. *StrålevernRapport 2013:2*, 2013.
- W. Josefsson and T. Landelius. Effect of clouds on uv irradiance: As estimated from cloud amount, cloud type, precipitation, global radiation and sunshine duration. *Journal of Geophysical Research: Atmospheres*, 105(D4):4927–4935, 2000.
- S. Kato, T. P. Ackerman, J. H. Mather, and E. E. Clothiaux. The k-distribution method and correlated-k approximation for a shortwave radiative transfer model. *Journal of Quantitative Spectroscopy and Radiative Transfer*, 62(1): 109–121, 1999.
- R. A. Kleinerman. Cancer risks following diagnostic and therapeutic radiation exposure in children. *Pediatric radiology*, 36(2):121–125, 2006.
- P. Koepke, J. Reuder, and H. Schwander. Solar uv radiation and its variability due to the atmospheric components. *Recent Res. Dev. Photochem. Photobiol*, 6(11):e34, 2002.
- H. Leenhouts and K. Chadwick. An analysis of synergistic sensitization. *The British journal of cancer. Supplement*, 3:198, 1978.
- J. Lenoble, A. Kylling, and I. Smolskaia. Impact of snow cover and topography on ultraviolet irradiance at the alpine station of briançon. *Journal of Geophysical Research: Atmospheres*, 109(D16), 2004.
- C. M. Lerche, P. A. Philipsen, and H. C. Wulf. X-rays and photocarcinogenesis in hairless mice. *Archives of dermatological research*, 305(6):529–533, 2013.
- A. Lindfors, J. Kaurola, A. Arola, T. Koskela, K. Lakkala, W. Josefsson, J. A. Olseth, and B. Johnsen. A method for reconstruction of past uv radiation based on radiative transfer modeling: Applied to four stations in northern europe. *Journal of Geophysical Research: Atmospheres*, 112(D23), 2007.
- R. Maryon, F. Smith, B. Conway, and D. Goddard. The uk nuclear accident model. *Progress in nuclear energy*, 26(2):85–104, 1991.
- B. Mayer, A. Kylling, C. Emde, U. Hamann, and R. Buras. libradtran user’s guide. *Edition for libRadtran version*, 1, 2012.
- R. McKenzie, K. Paulin, and S. Madronich. Effects of snow cover on uv irradiance and surface albedo. *JOURNAL OF GEOPHYSICAL RESEARCH-ALL SERIES-*, 103:28–785, 1998.

- F. A. Mettler Jr, A. K. Gus'kova, and I. Gusev. Health effects in those with acute radiation sickness from the chernobyl accident. *Health physics*, 93(5): 462–469, 2007.
- M. F. Naylor. Erythema, skin cancer risk, and sunscreens. *Archives of dermatology*, 133(3):373–375, 1997.
- NRPA. Protective measures in early and intermediate phases of a nuclear or radiological emergency: Nordic guidelines and recommendations. Technical report, Danish Emergency Management Agency, National Institute of Radiation Protection, Icelandic Radiation Safety Authority, Radiation and Nuclear Safety Authority, Swedish Radiation Safety Authority, 2014.
- R. Quinn. Sellafield 'riddled with safety flaws', according to bbc investigation, 2016. URL <https://www.theguardian.com/environment/2016/sep/05/sellafield-nuclear-plant-riddled-safety-flaws-according-bbc-panorama>.
- R. A. Rohde. Solar spectrum, 2007. URL https://commons.wikimedia.org/wiki/File:Solar_Spectrum.png. [Online; accessed March 09, 2017].
- C. Roméro-Graillet, E. Aberdam, M. Clément, J.-P. Ortonne, and R. Ballotti. Nitric oxide produced by ultraviolet-irradiated keratinocytes stimulates melanogenesis. *Journal of Clinical Investigation*, 99(4):635, 1997.
- SCCP. Opinion on biological effects of ultraviolet radiation relevant to health with particular reference to sunbeds for cosmetic purposes. 2006.
- E. P. Shettle. Models of aerosols, clouds, and precipitation for atmospheric propagation studies. In *In AGARD, Atmospheric Propagation in the UV, Visible, IR, and MM-Wave Region and Related Systems Aspects 14 p (SEE N90-21907 15-32)*, volume 1, 1990.
- K. Stamnes, S.-C. Tsay, W. Wiscombe, and I. Laszlo. Disort, a general-purpose fortran program for discrete-ordinate-method radiative transfer in scattering and emitting layered media: documentation of methodology. *Goddard Space Flight Center, NASA*, 2000.
- G. E. Thomas and K. Stamnes. *Radiative transfer in the atmosphere and ocean*. Cambridge University Press, 2002.
- D. E. Thompson, K. Mabuchi, E. Ron, M. Soda, M. Tokunaga, S. Ochikubo, S. Sugimoto, T. Ikeda, M. Terasaki, S. Izumi, et al. Cancer incidence in atomic bomb survivors. part ii: Solid tumors, 1958-1987. *Radiation research*, 137(2s):S17–S67, 1994.
- R. M. Tyrrell. Radiation synergism and antagonism. In *Photochemical and photobiological reviews*, pages 35–113. Springer, 1978.
- UNSCEAR. Sources and effects of ionizing radiation. unscar 1996 report to the general assembly, with scientific annex. 1996.
- M. Unterweger. Half-life measurements at the national institute of standards and technology. *Applied Radiation and Isotopes*, 56(1):125–130, 2002.

- A. R. Webb and O. Engelsen. Calculated ultraviolet exposure levels for a healthy vitamin d status. *Photochemistry and Photobiology*, 82(6):1697–1703, 2006.
- A. R. Webb, H. Slaper, P. Koepke, and A. W. Schmalwieser. Know your standard: clarifying the cie erythema action spectrum. *Photochemistry and photobiology*, 87(2):483–486, 2011.
- WHO. Global solar uv index: A practical guide. 2002.
- M. A. Ytre-Eide, W. J. Standring, I. Amundsen, M. Sickel, A. Liland, J. Saltbones, J. Bartnicki, H. Haakenstad, and B. Salbu. Consequences in norway of a hypothetical accident at sellafeld: potential release–transport and fallout. 2009.

Appendices

Appendix A

Daily UVI Plots for Fureneset, Flesland and Særheim

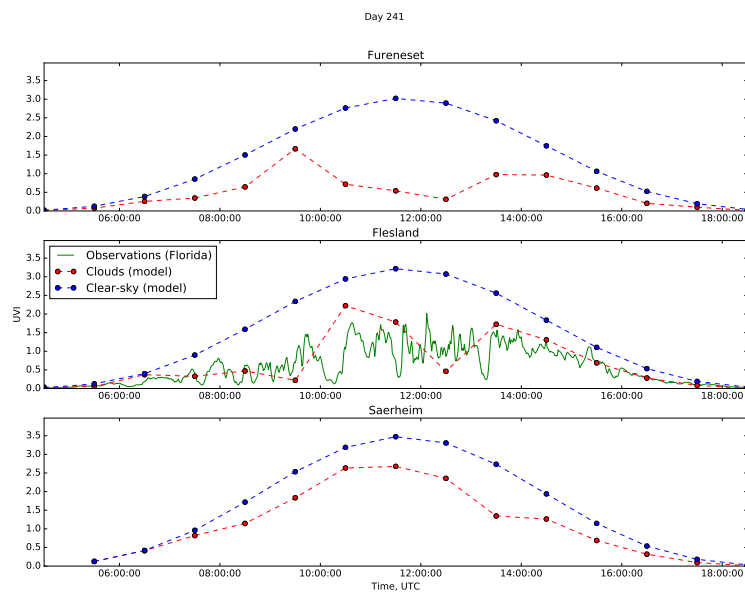


Figure A.1: Calculated UV Index for 29. August 2015.

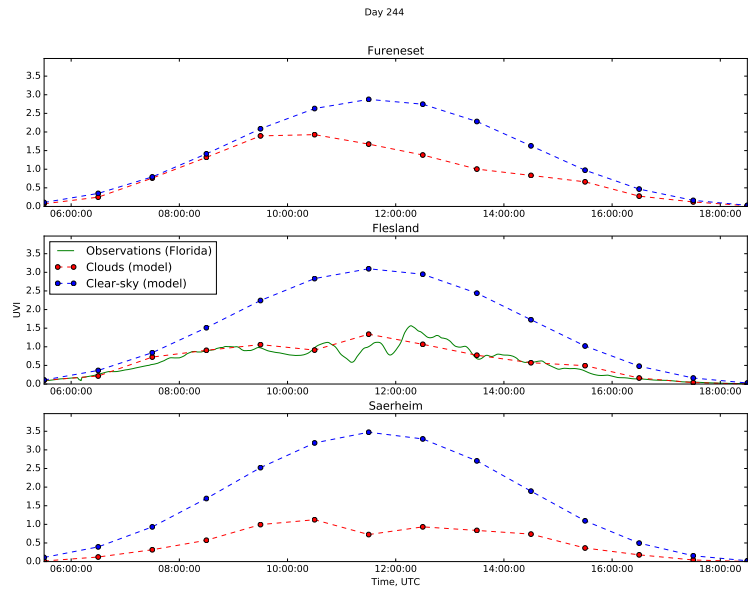


Figure A.2: Calculated UV Index for 1. September 2015.

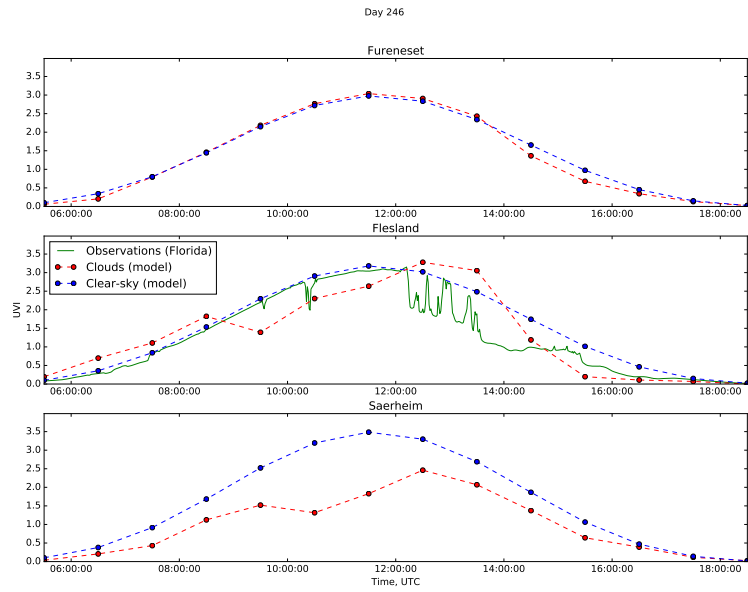


Figure A.3: Calculated UV Index for 3. September 2015.

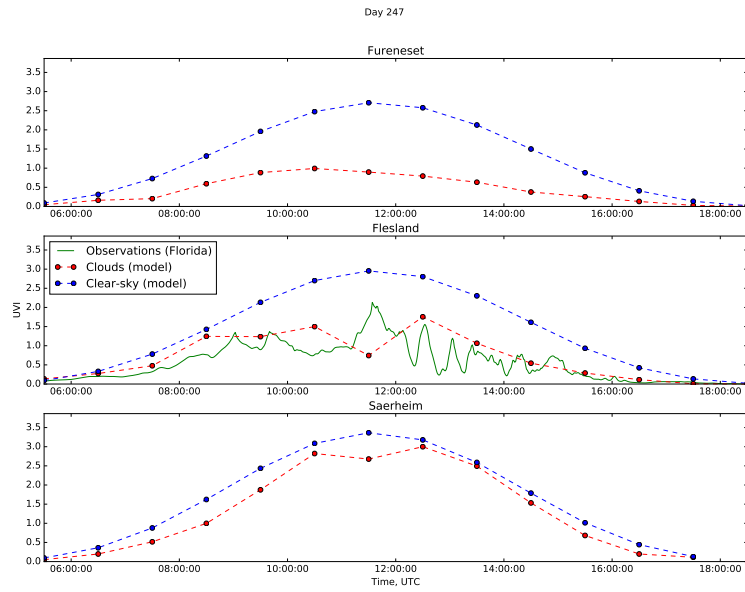


Figure A.4: Calculated UV Index for 4. September 2015.

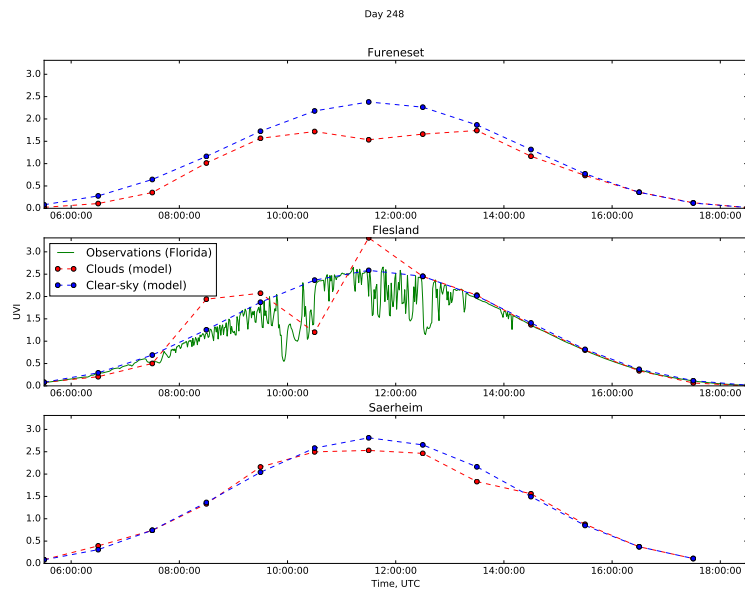


Figure A.5: Calculated UV Index for 5. September 2015.

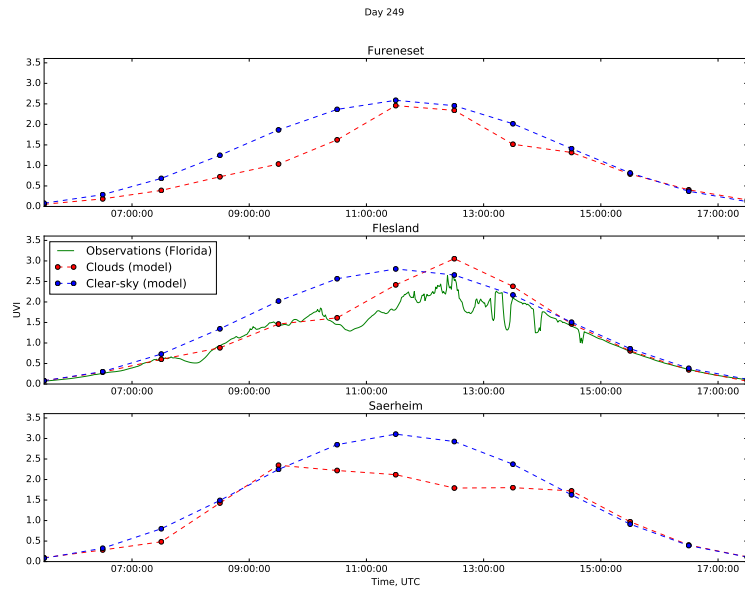


Figure A.6: Calculated UV Index for 6. September 2015.

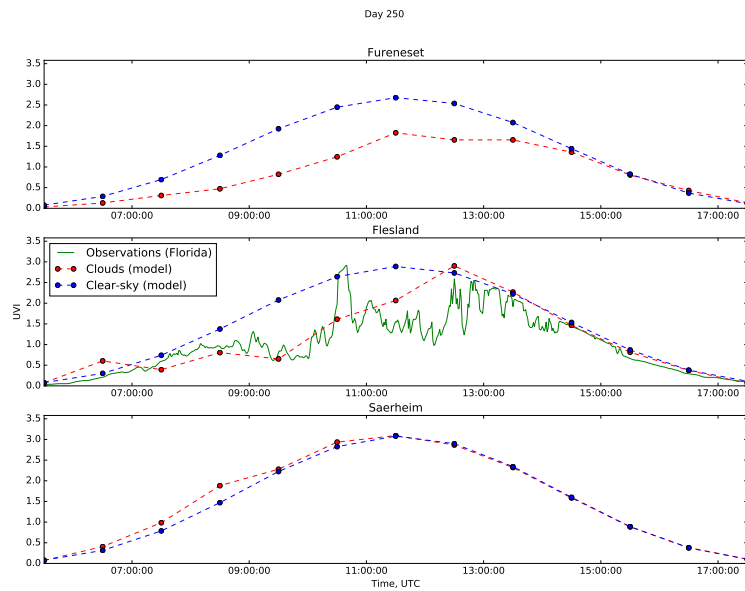


Figure A.7: Calculated UV Index for 7. September 2015.

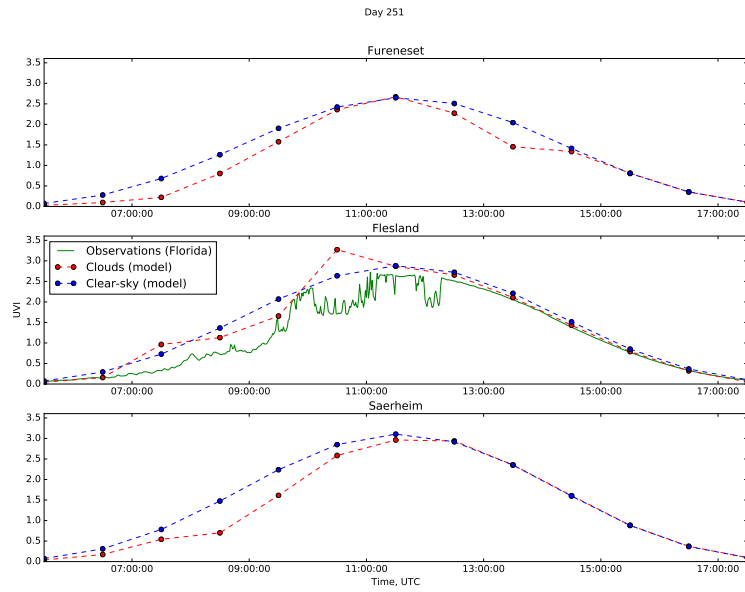


Figure A.8: Calculated UV Index for 8. September 2015.

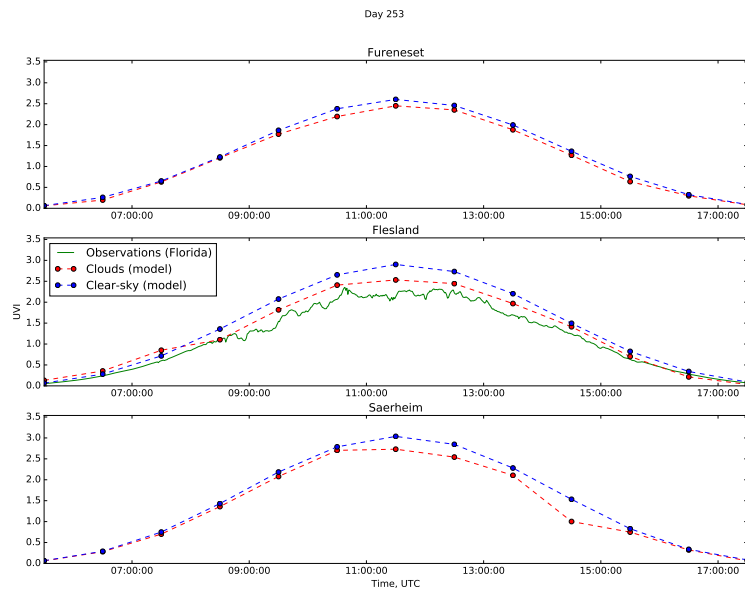


Figure A.9: Calculated UV Index for 10. September 2015.

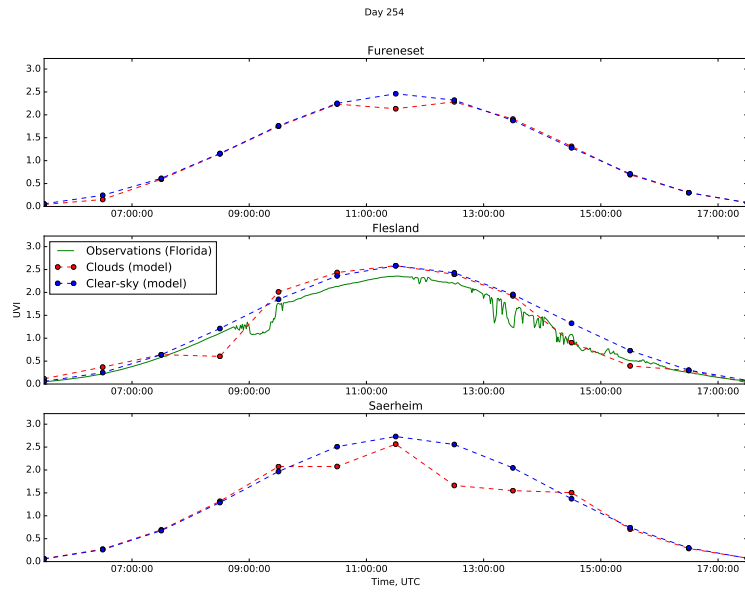


Figure A.10: Calculated UV Index for 11. September 2015.

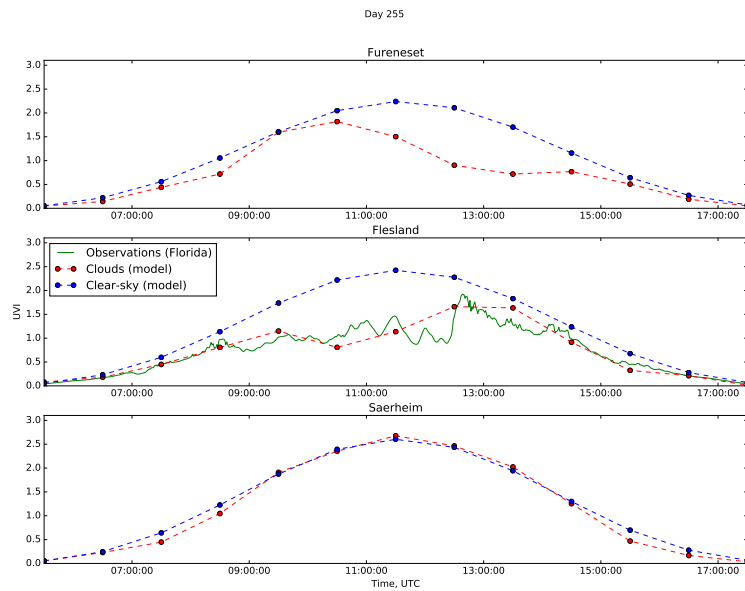


Figure A.11: Calculated UV Index for 12. September 2015.

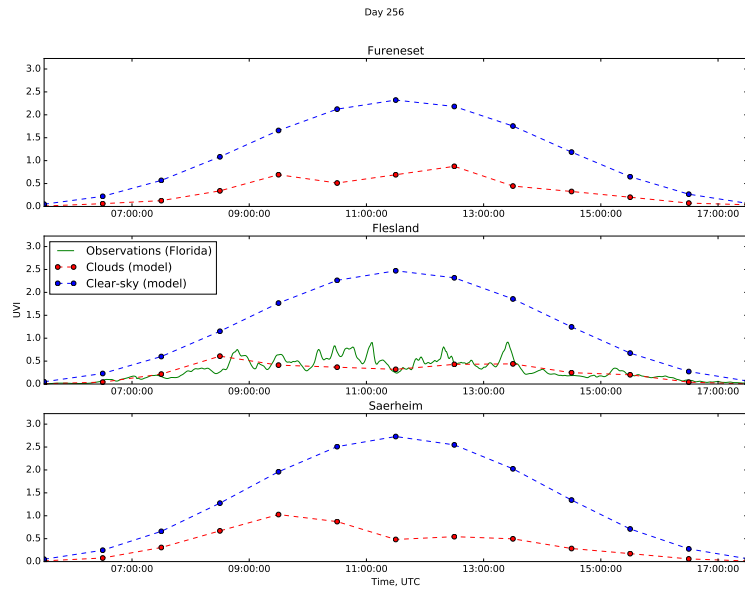


Figure A.12: Calculated UV Index for 13. September 2015.

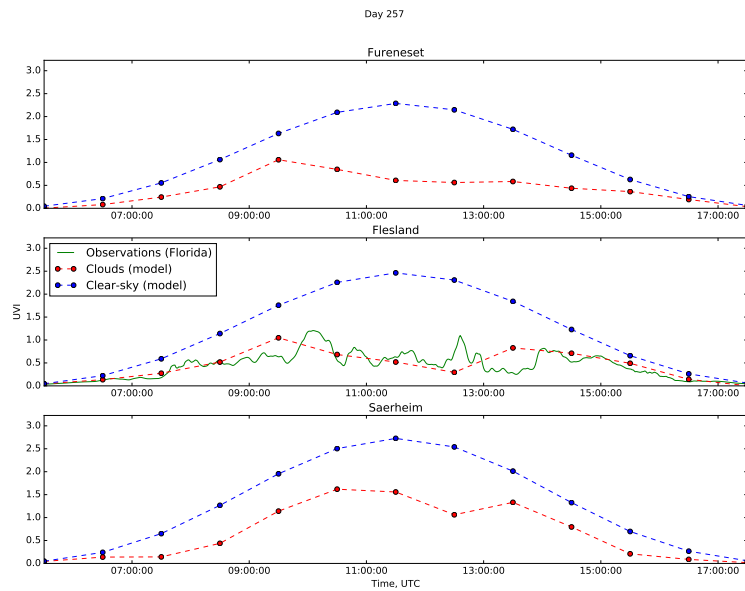


Figure A.13: Calculated UV Index for 14. September 2015.

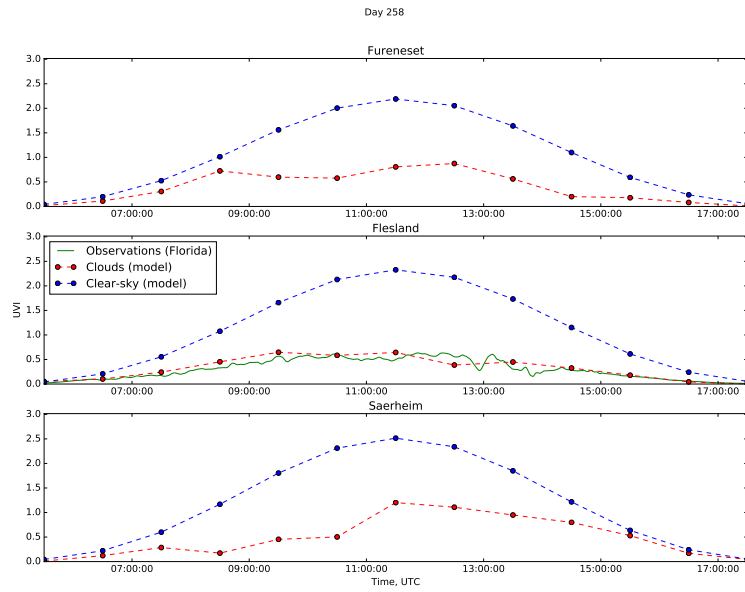


Figure A.14: Calculated UV Index for 15. September 2015.

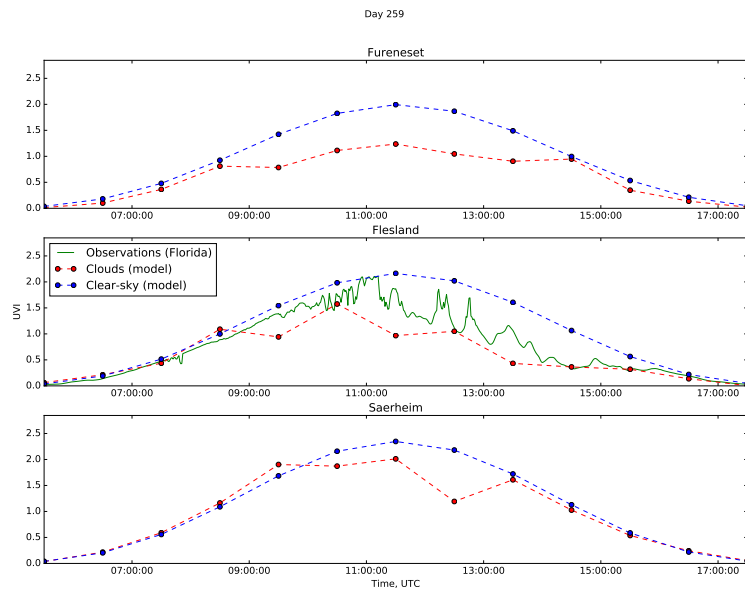


Figure A.15: Calculated UV Index for 16. September 2015.

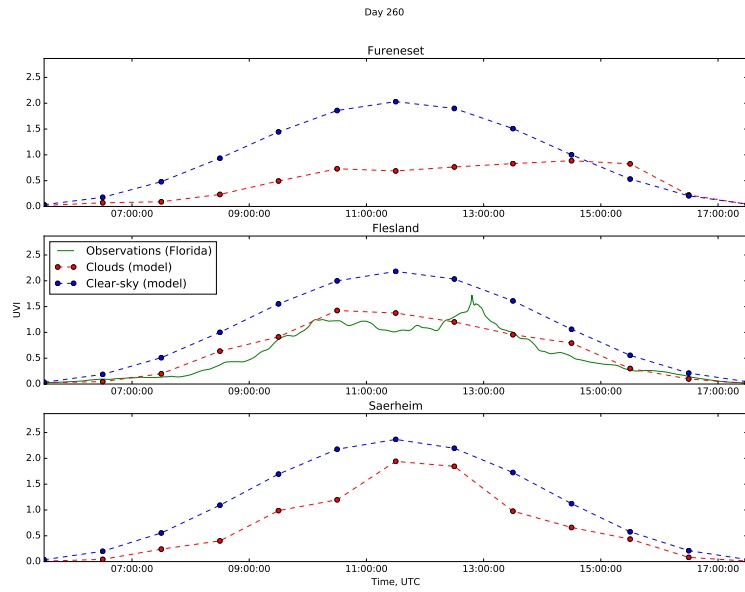


Figure A.16: Calculated UV Index for 17. September 2015.

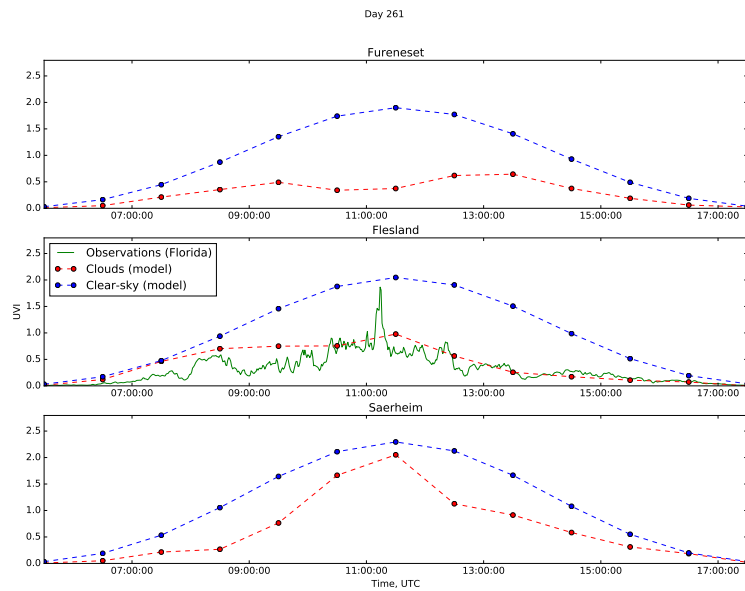


Figure A.17: Calculated UV Index for 18. September 2015.

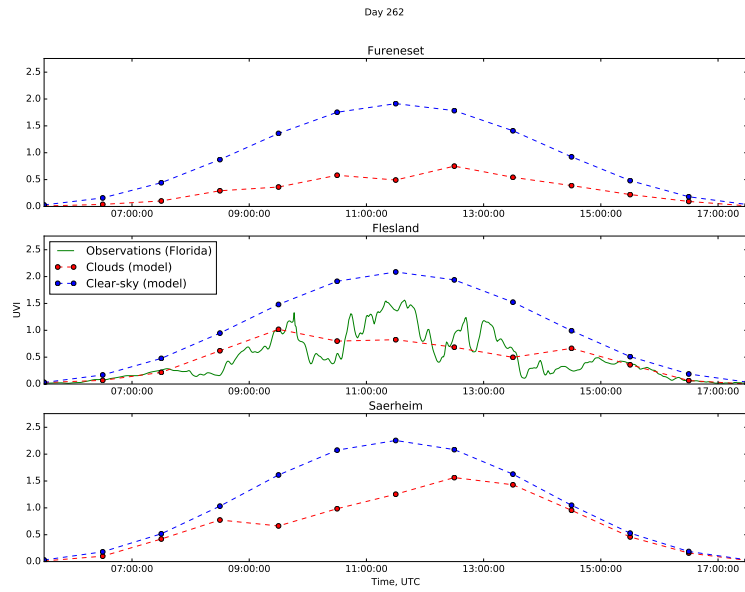


Figure A.18: Calculated UV Index for 19. September 2015.

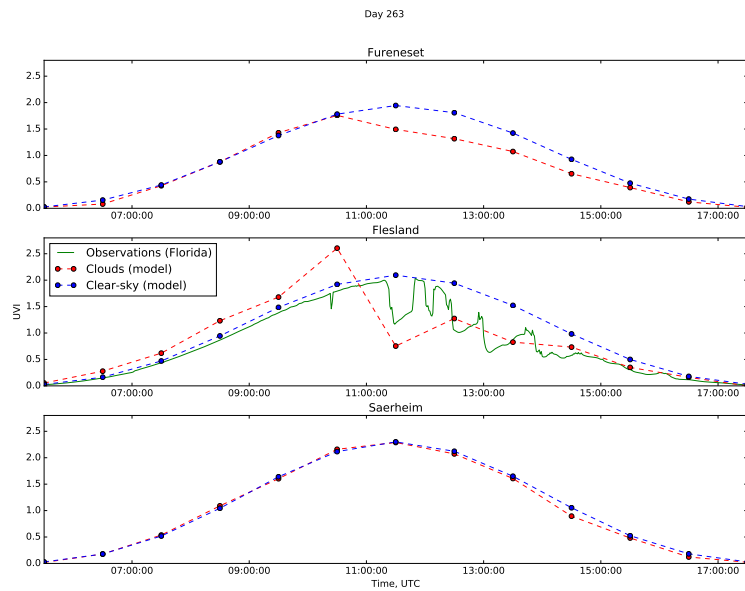


Figure A.19: Calculated UV Index for 20. September 2015.

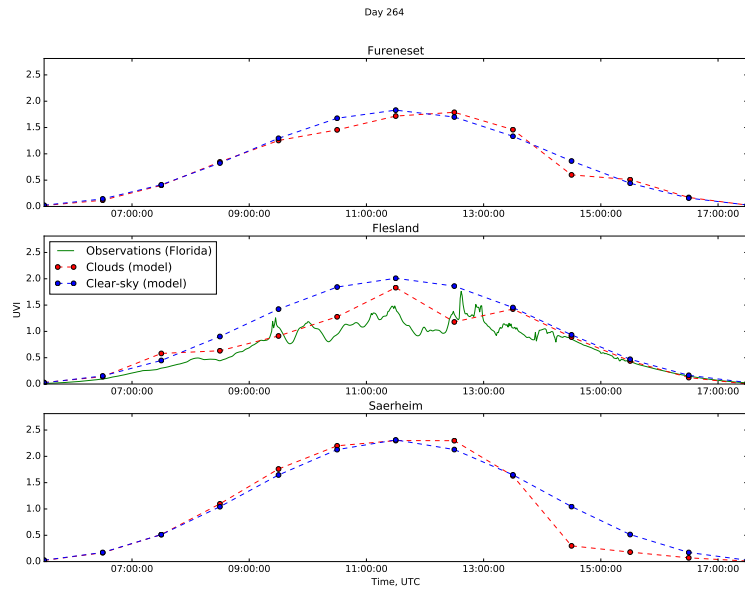


Figure A.20: Calculated UV Index for 21. September 2015.

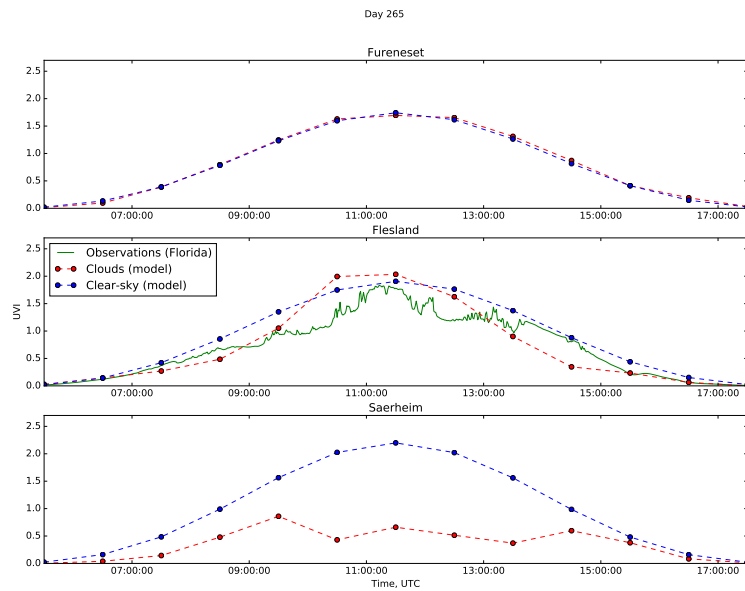


Figure A.21: Calculated UV Index for 22. September 2015.

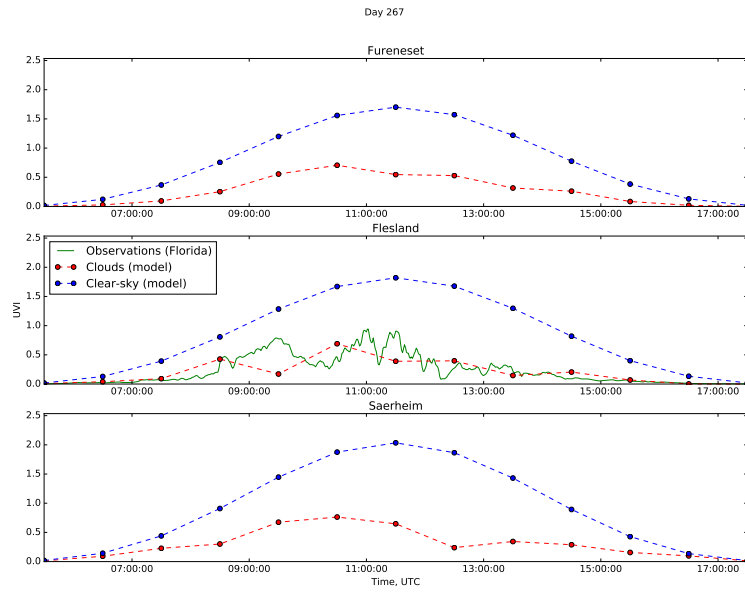


Figure A.22: Calculated UV Index for 24. September 2015.

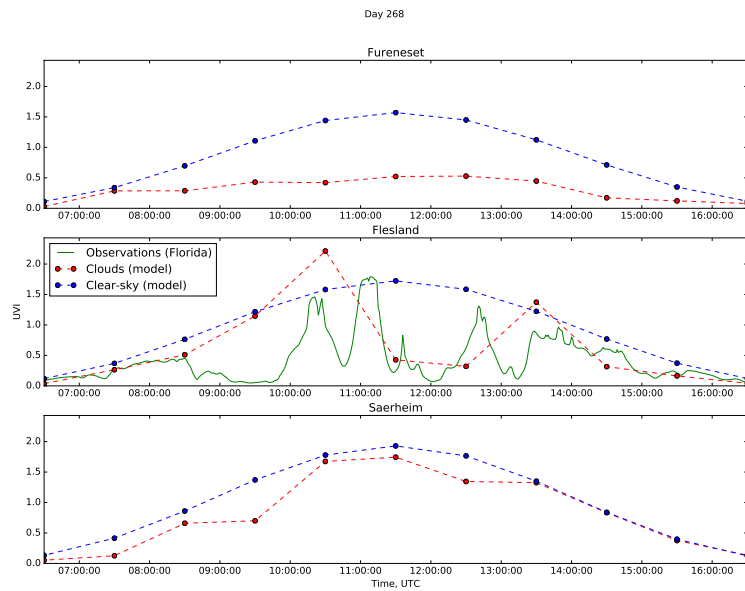


Figure A.23: Calculated UV Index for 25. September 2015.

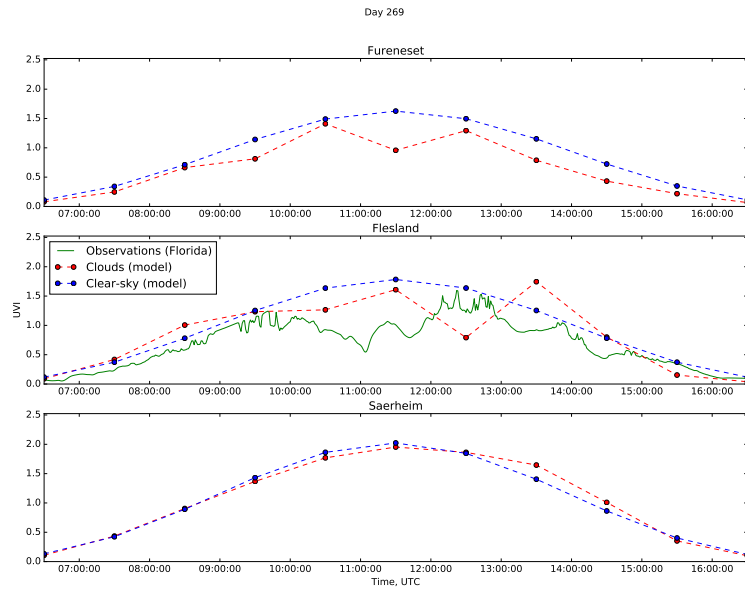


Figure A.24: Calculated UV Index for 26. September 2015.

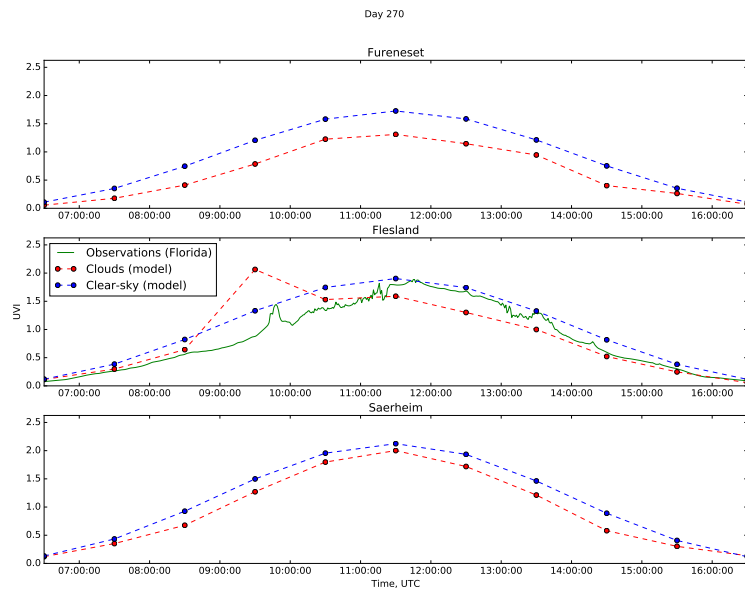


Figure A.25: Calculated UV Index for 27. September 2015.

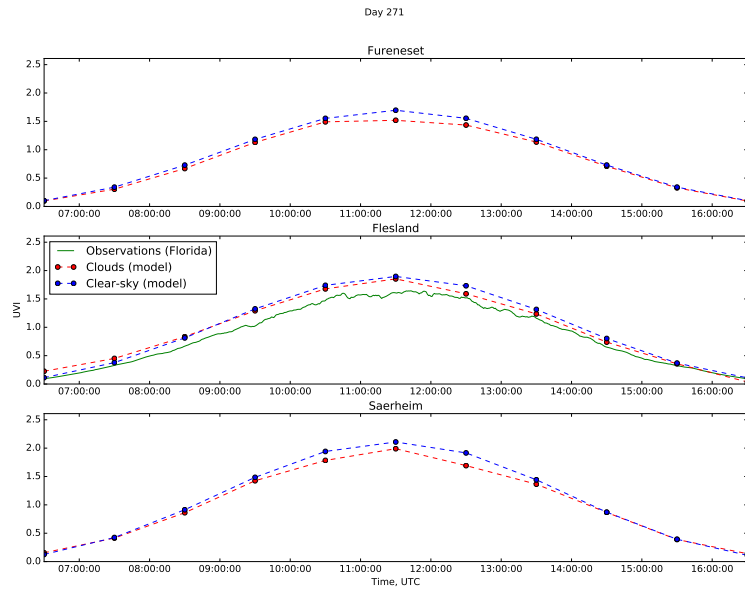


Figure A.26: Calculated UV Index for 28. September 2015.

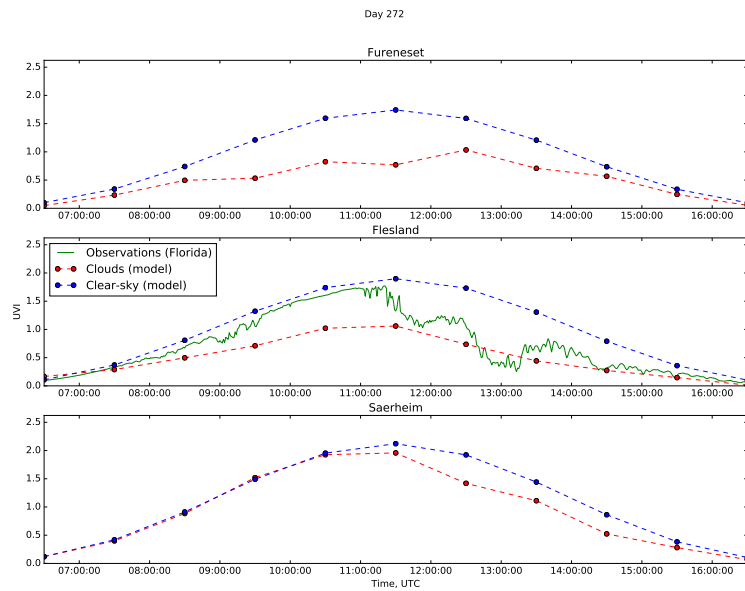


Figure A.27: Calculated UV Index for 29. August 2015.

Appendix B

Daily UVI Plots for Florida

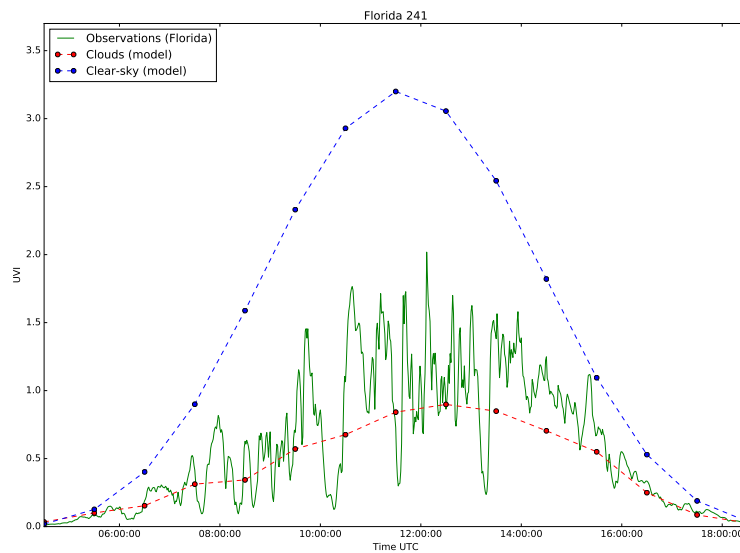


Figure B.1: Calculated UV Index for 29. August 2015.

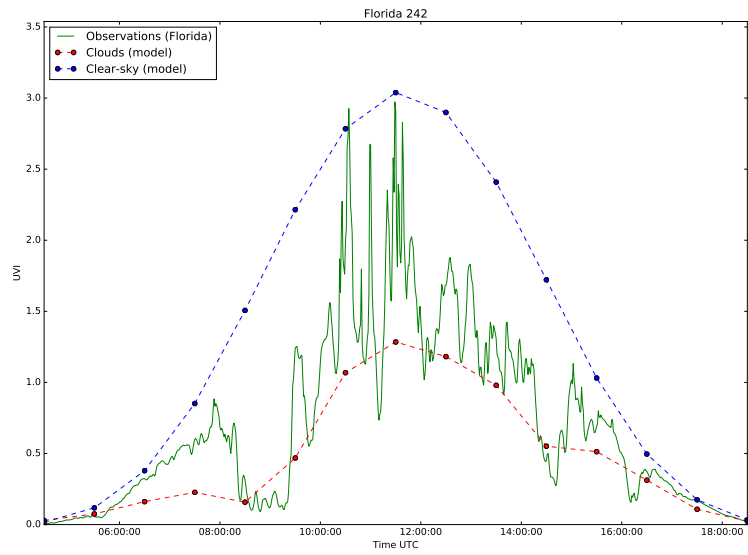


Figure B.2: Calculated UV Index for 30. August 2015.

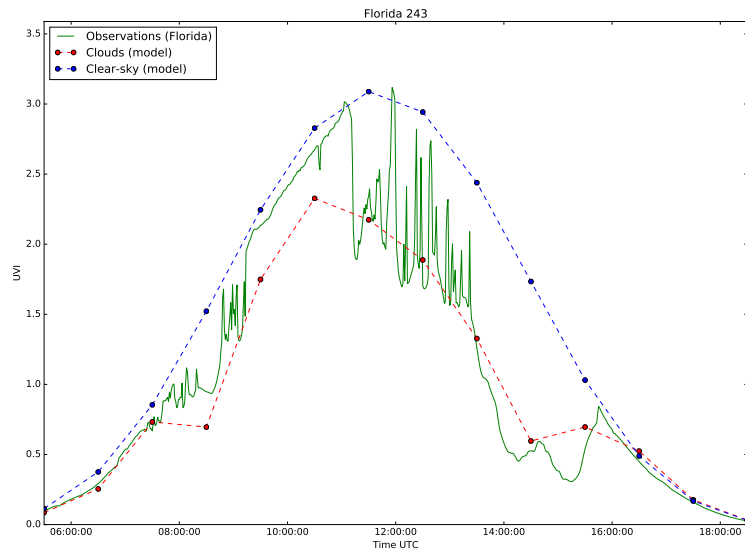


Figure B.3: Calculated UV Index for 31. August 2015.

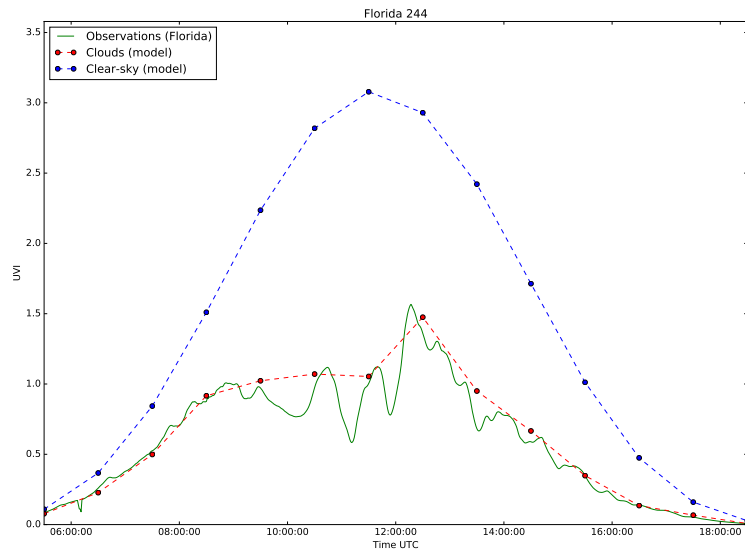


Figure B.4: Calculated UV Index for 1. September 2015.

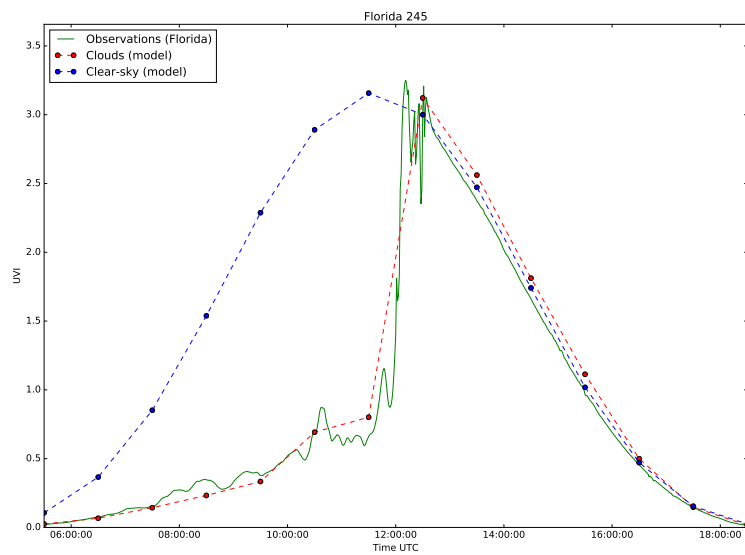


Figure B.5: Calculated UV Index for 2. September 2015.

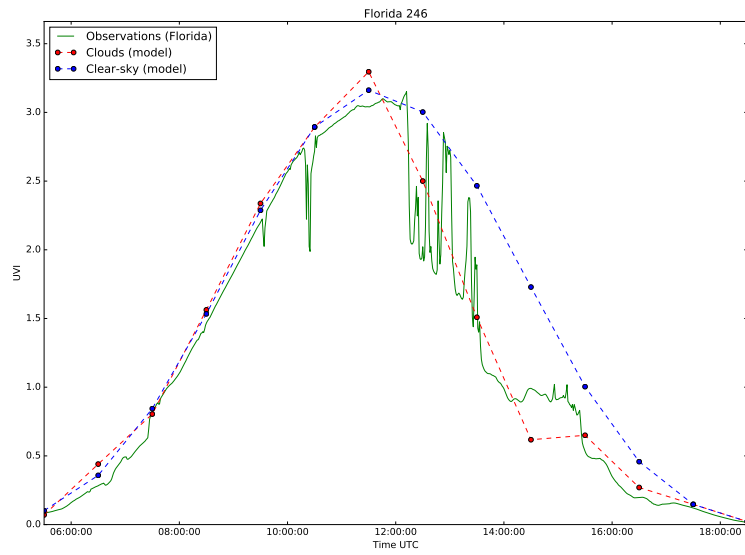


Figure B.6: Calculated UV Index for 3. September 2015.

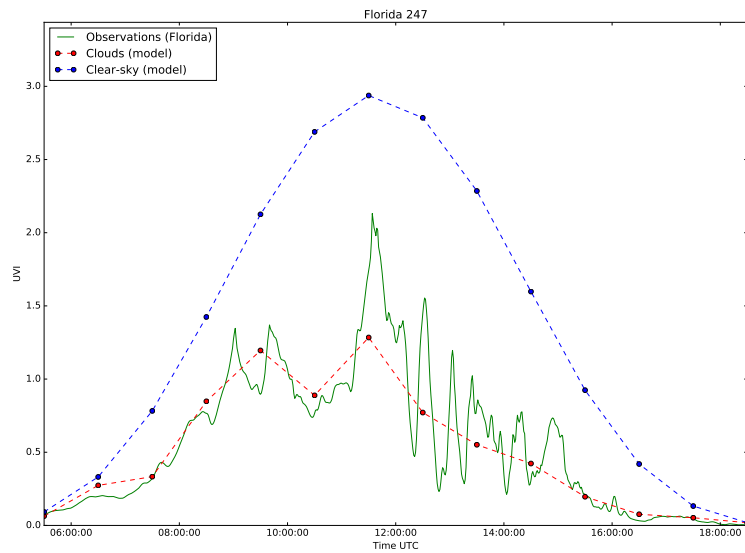


Figure B.7: Calculated UV Index for 4. September 2015.

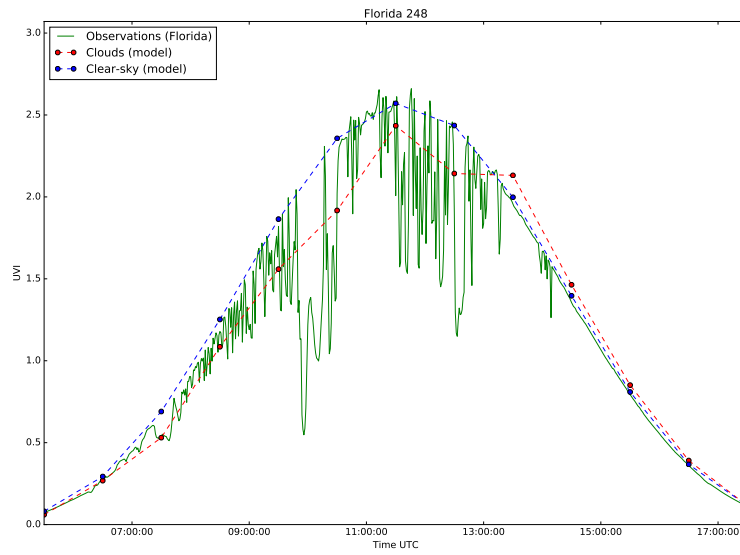


Figure B.8: Calculated UV Index for 5. September 2015.

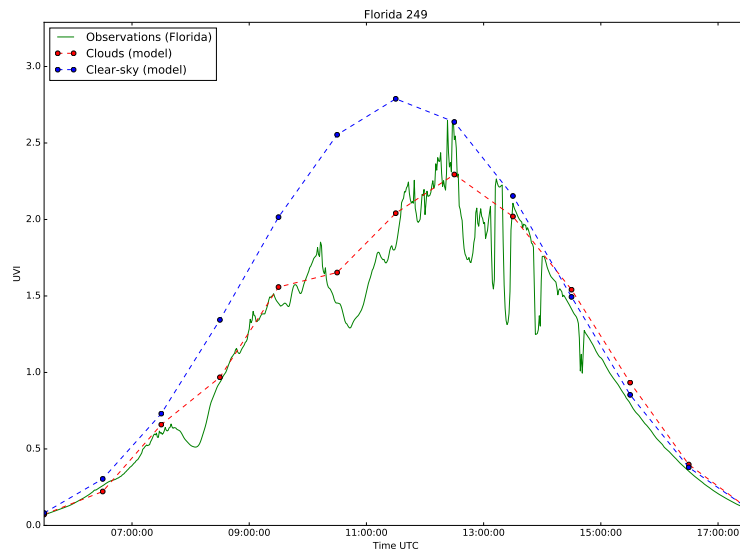


Figure B.9: Calculated UV Index for 6. September 2015.

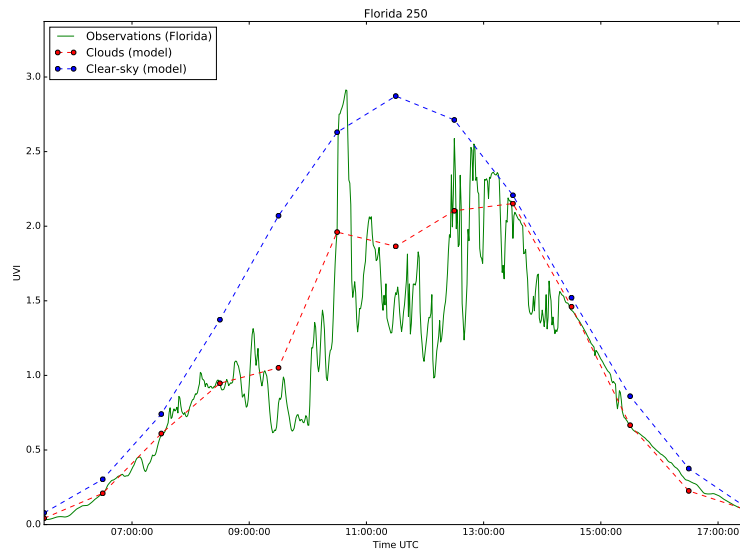


Figure B.10: Calculated UV Index for 7. September 2015.

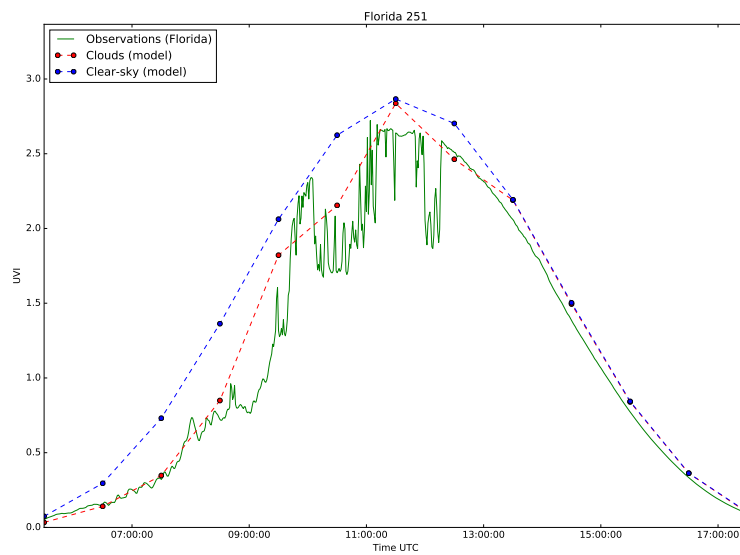


Figure B.11: Calculated UV Index for 8. September 2015.

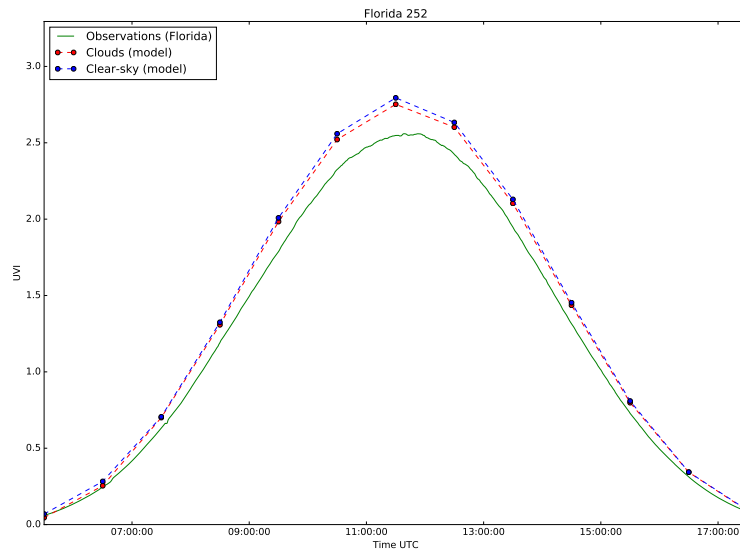


Figure B.12: Calculated UV Index for 9. September 2015.

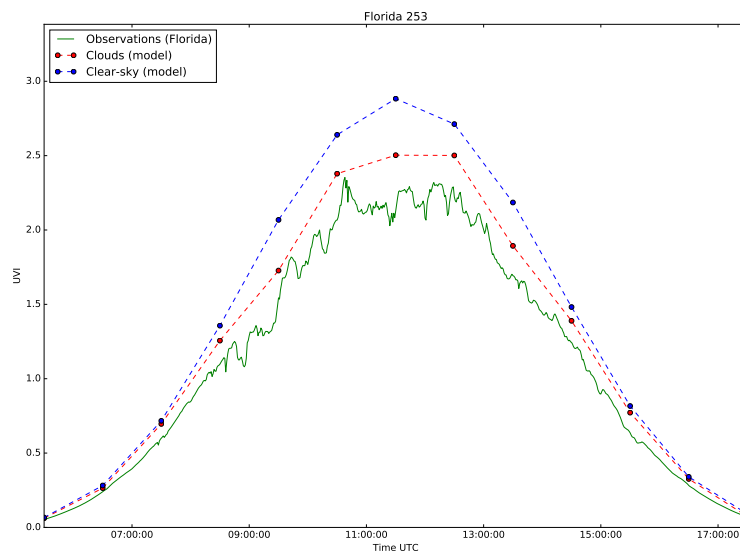


Figure B.13: Calculated UV Index for 10. September 2015.

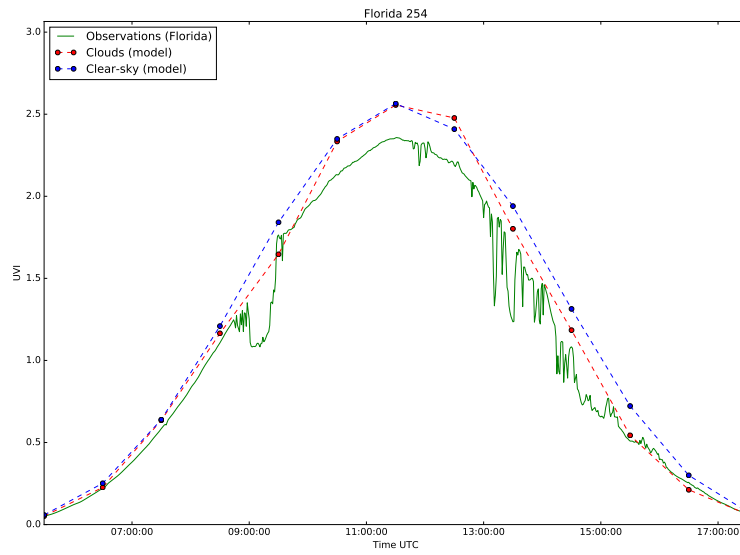


Figure B.14: Calculated UV Index for 11. September 2015.

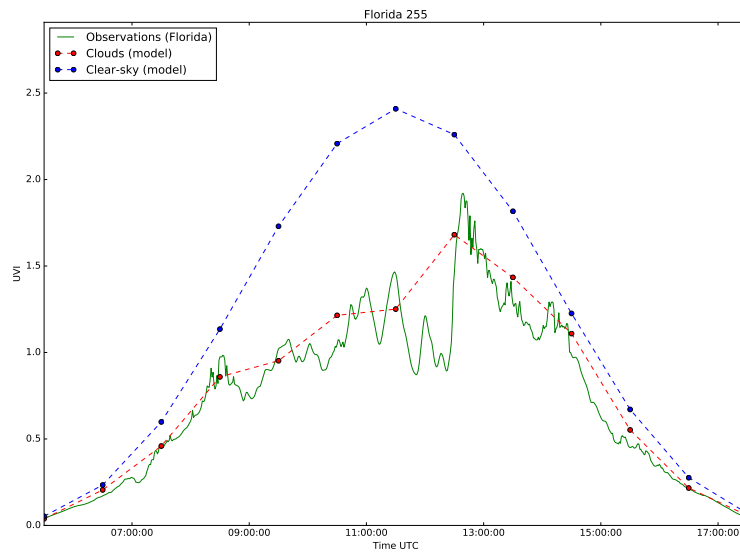


Figure B.15: Calculated UV Index for 12. September 2015.

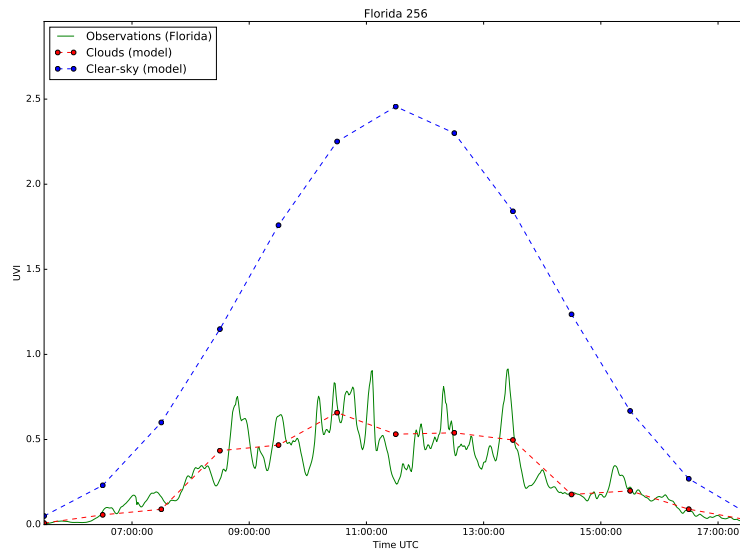


Figure B.16: Calculated UV Index for 13. September 2015.

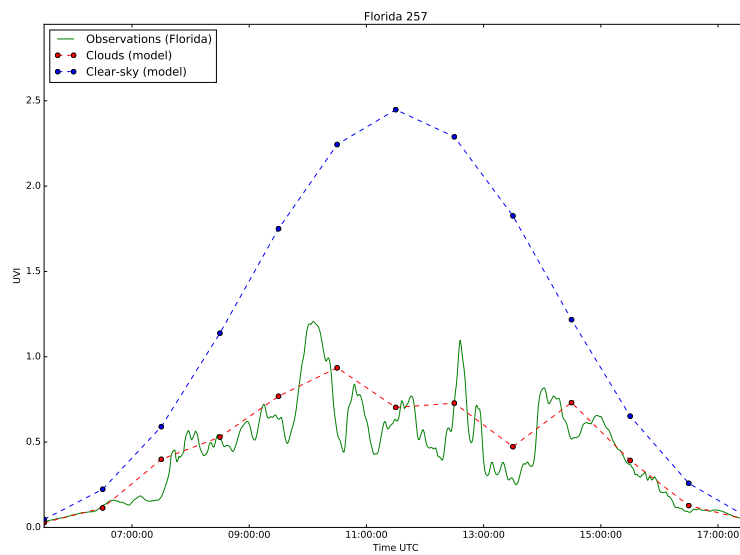


Figure B.17: Calculated UV Index for 14. September 2015.

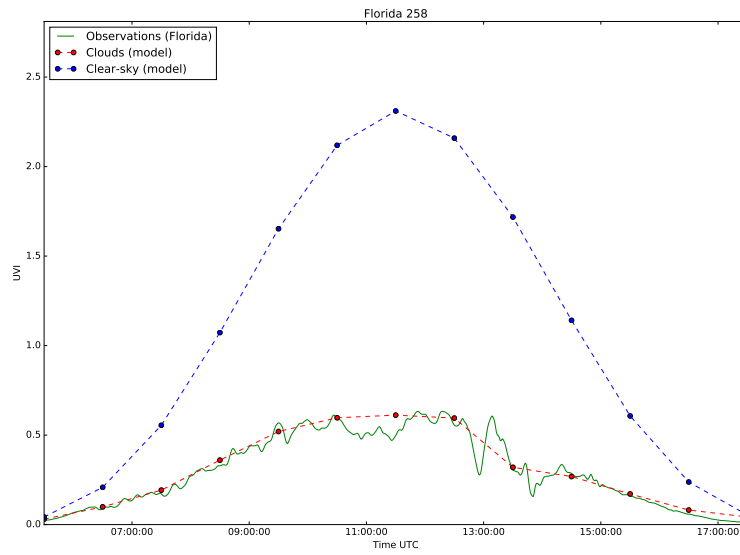


Figure B.18: Calculated UV Index for 15. September 2015.

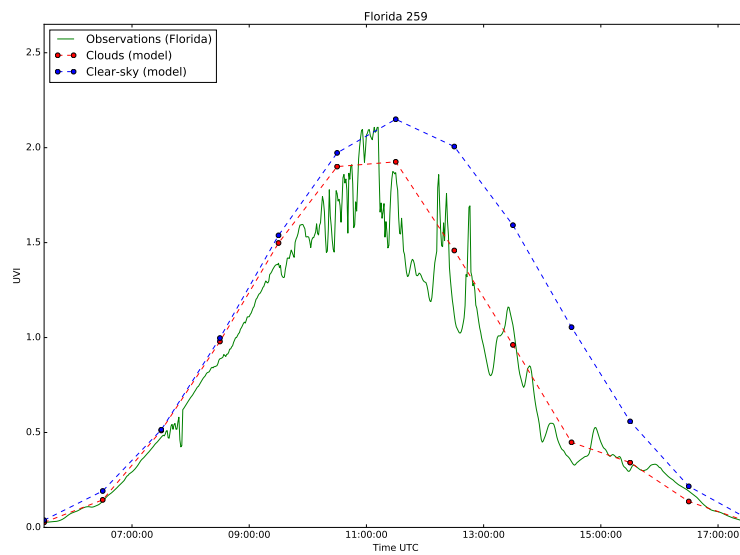


Figure B.19: Calculated UV Index for 16. September 2015.

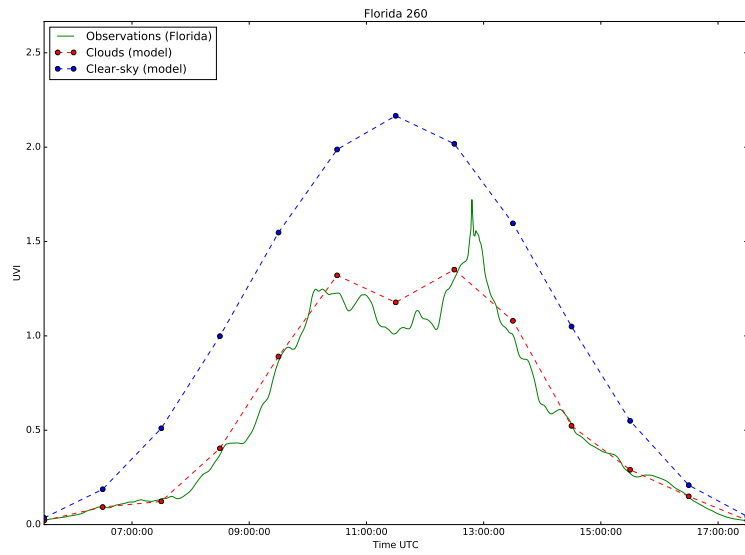


Figure B.20: Calculated UV Index for 17. September 2015.

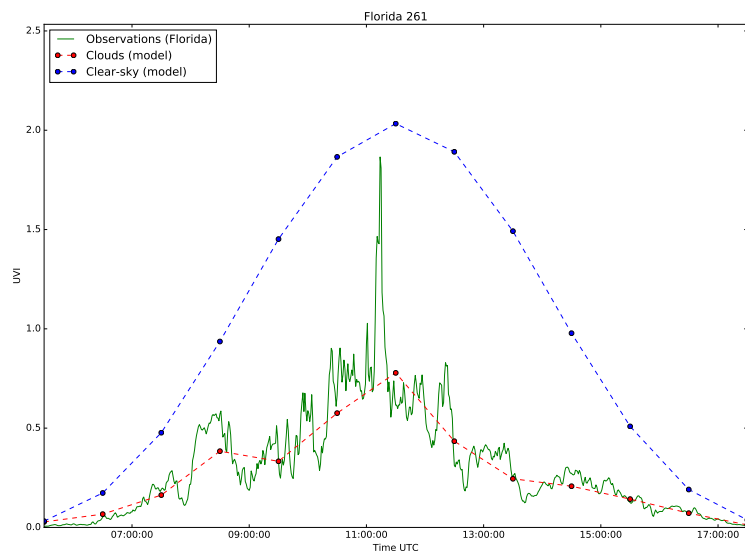


Figure B.21: Calculated UV Index for 18. September 2015.

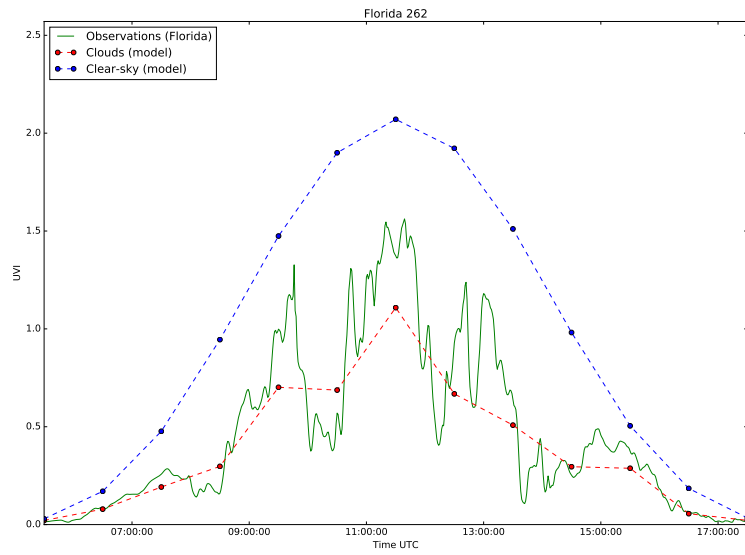


Figure B.22: Calculated UV Index for 19. September 2015.

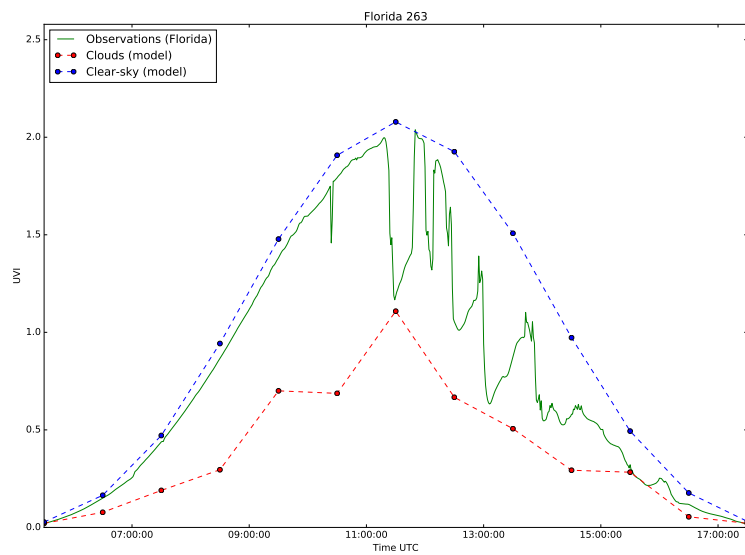


Figure B.23: Calculated UV Index for 20. September 2015.

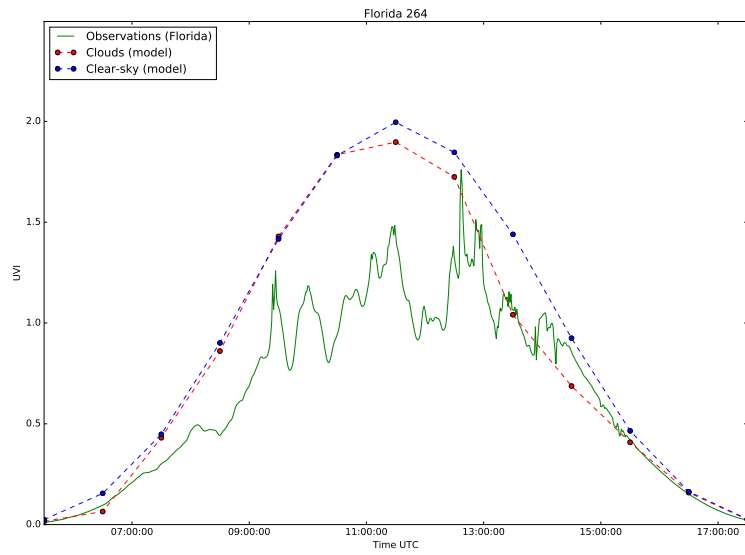


Figure B.24: Calculated UV Index for 21. September 2015.

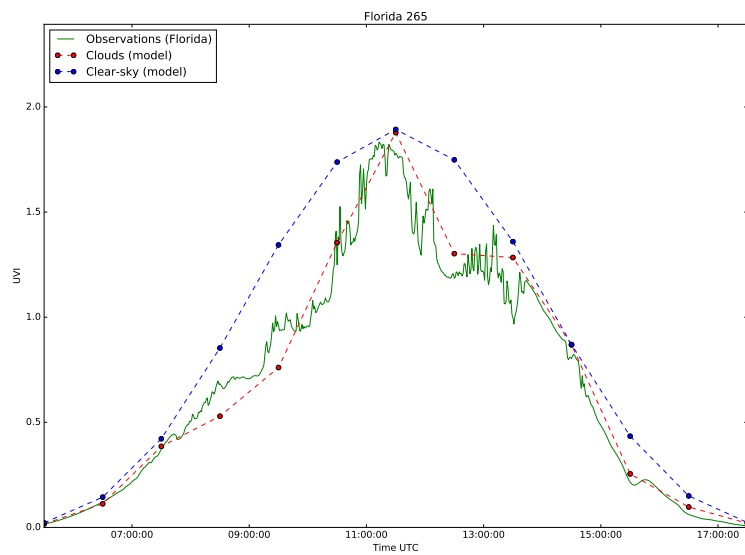


Figure B.25: Calculated UV Index for 22. September 2015.

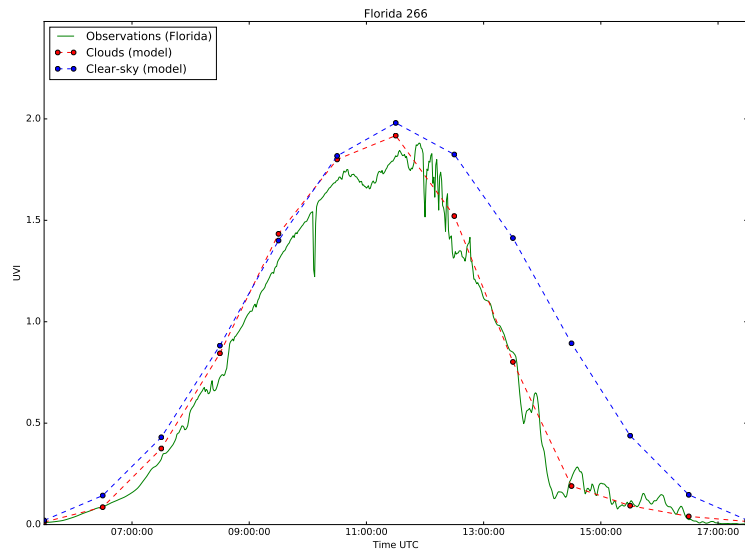


Figure B.26: Calculated UV Index for 23. September 2015.

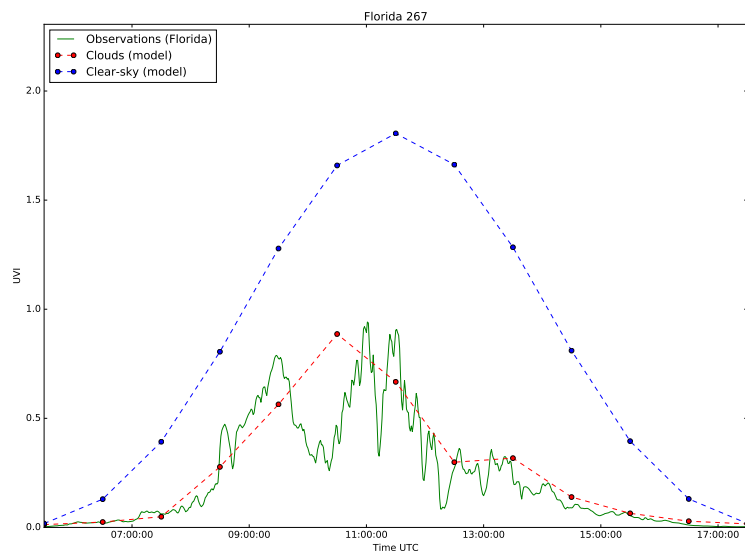


Figure B.27: Calculated UV Index for 24. September 2015.

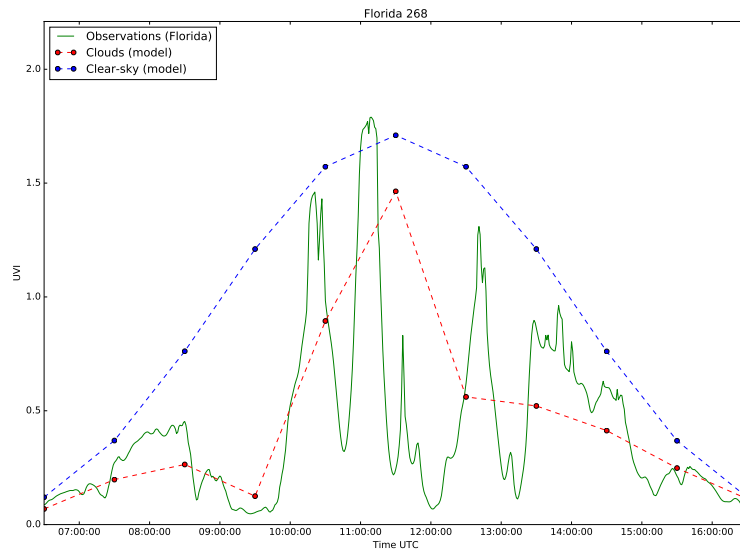


Figure B.28: Calculated UV Index for 25. September 2015.

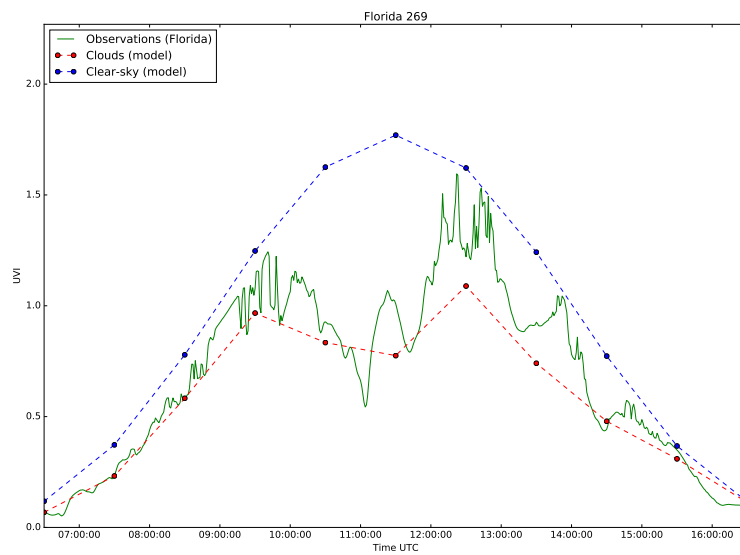


Figure B.29: Calculated UV Index for 26. September 2015.

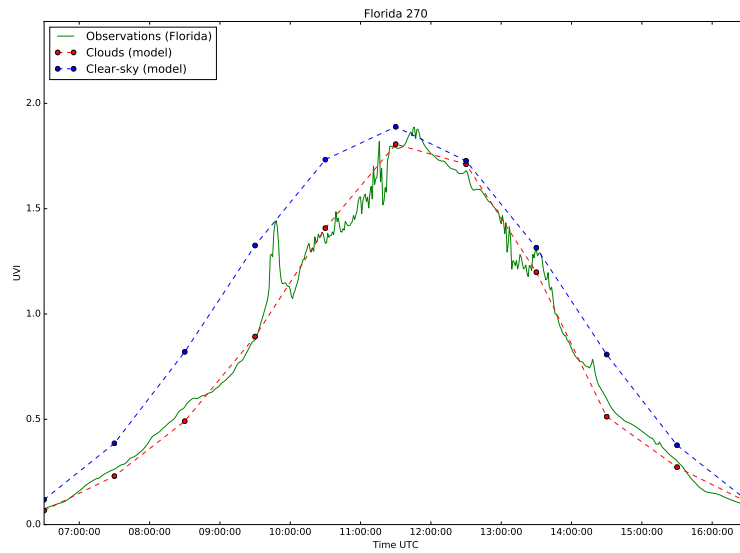


Figure B.30: Calculated UV Index for 27. September 2015.

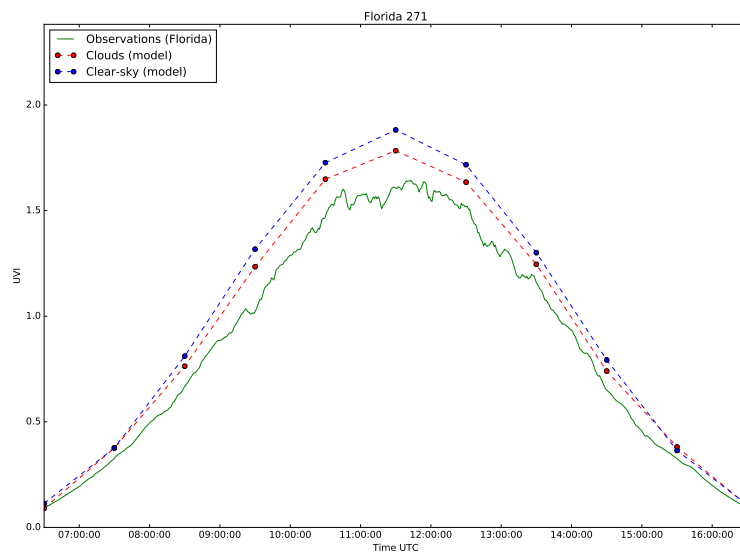


Figure B.31: Calculated UV Index for 28. September 2015.

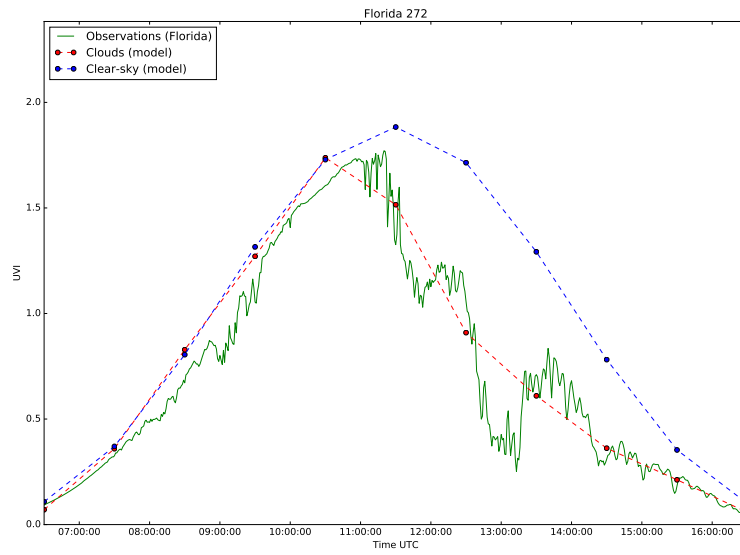


Figure B.32: Calculated UV Index for 29. September 2015.